

1 **Phytochemical-loaded mesoporous silica nanoparticles for nose-to-brain olfactory drug**
2 **delivery**

3

4

5

6 **Shital Lungare¹, Keith Hallam², Raj K. S. Badhan¹**

7 ¹ Aston Pharmacy School, Life and Health Sciences, Aston University, Birmingham, B4 7ET,
8 United Kingdom.

9 ² Interface Analysis Centre, School of Physics, University of Bristol, Bristol BS8 1TL,
10 United Kingdom.

11

12 **Correspondence:**

13 Dr Raj K. Singh Badhan

14 Aston Pharmacy School

15 Life and Health Sciences

16 Aston University

17 Birmingham

18 B4 7ET

19 UK

20 Telephone: +44 121 204 3288

21 Fax: +44 121 204 3000

22 E-mail: r.k.s.badhan@aston.ac.uk

23

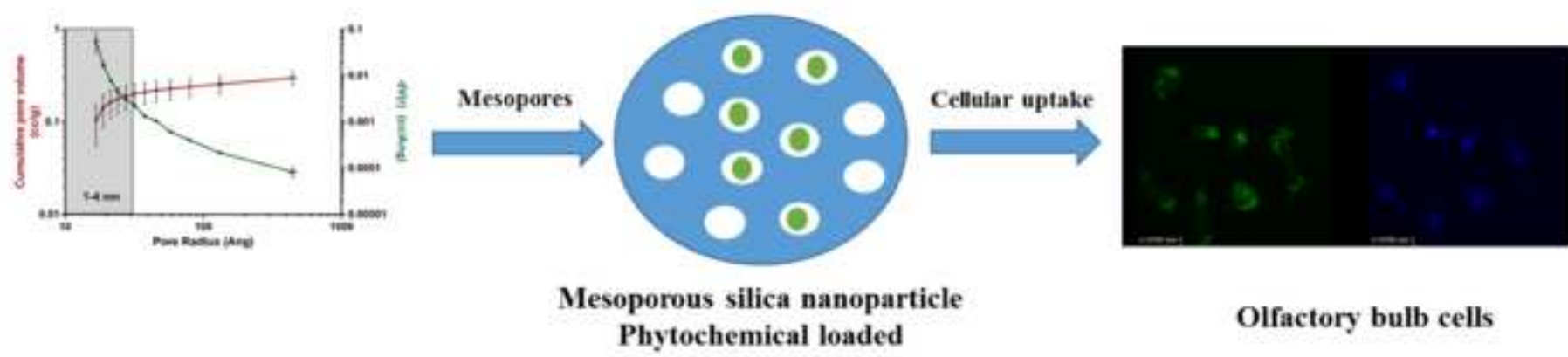
24 **ABSTRACT**

25 Central nervous system (CNS) drug delivery is often hampered due to the insidious nature of
26 the blood-brain barrier (BBB). Nose-to-brain delivery *via* olfactory pathways have become a
27 target of attention for drug delivery due to bypassing of the BBB. The antioxidant properties
28 of phytochemicals make them promising as CNS active agents but possess poor water
29 solubility and limited BBB penetration. The primary aim of this study was the development
30 of mesoporous silica nanoparticles (MSNs) loaded with the poorly water-soluble
31 phytochemicals curcumin and chrysin which could be utilised for nose-to-brain delivery. We
32 formulated spherical MSNP using a templating approach resulting in ~220 nm particles with
33 a high surface porosity. Curcumin and chrysin were successfully loaded into MSNP and
34 confirmed through Fourier transformation infrared spectroscopy (FT-IR), differential
35 scanning calorimetry (DSC), thermogravimetric analysis (TGA) and HPLC approaches with
36 a loading of 11-14% for curcumin and chrysin. Release was pH dependant with curcumin
37 demonstrating increased chemical stability at a lower pH (5.5) with a release of $53.2 \% \pm 2.2$
38 % over 24 hours and $9.4 \pm 0.6 \%$ for chrysin. MSNP were demonstrated to be non-toxic to
39 olfactory neuroblastoma cells OBGF400, with chrysin (100 μM) demonstrating a decrease in
40 cell viability to $58.2 \pm 8.5 \%$ and curcumin an IC_{50} of $33 \pm 0.18 \mu\text{M}$. Furthermore confocal
41 microscopy demonstrated nanoparticles of $< 500\text{nm}$ were able to accumulate within cells
42 with FITC-loaded MSNP showing membrane localised and cytoplasmic accumulation
43 following a 2-hour incubation. MSNP are useful carriers for poorly soluble phytochemicals
44 and provide a novel vehicle to target and deliver drugs into the CNS and bypass the BBB
45 through olfactory drug delivery.

46

47 **KEYWORDS**

48 Mesoporous silica nanoparticle; olfactory; nose-to-brain; flavonoid; phytochemical.



49 1. INTRODUCTION

50 The World Health Organisation (WHO) have highlighted that neurological disorders are one
51 of the biggest threats to public health ¹. Disorders of the CNS account for approximately 1 %
52 of deaths but this is associated with a worldwide disease burden of almost 11 %, and it is
53 thought that approximately 1.5 billion people worldwide suffer from some kind of brain or
54 CNS disorder ¹. Furthermore with an increasingly ageing population, by the year 2020 one
55 in every three people alive will suffer from a central nervous system (CNS) related disorder ¹.

56 Similar paradigms exist within the pharmaceutical industry with less than 8 % of CNS-
57 indicated drugs successfully enter clinical trials and accompanied by an overall drop in the
58 success rate of delivering a candidate to market ², with the US Food and Drug Administration
59 (FDA) only approving between 15-25 new compounds per year ². Despite advances in drug
60 delivery technologies, CNS drug targeting and delivery is still a limiting factor with less than
61 1 % of all CNS-targeted compounds showing activity against CNS diseases ^{3,4}. This is
62 despite many of these compounds possessing physicochemical properties that would
63 normally predispose them to good membrane permeability (e.g, molecular weight < 500 and
64 highly lipid soluble) ⁵. The brain is a very highly vascularised organ with a microvascular
65 surface area of 150-200 cm² g. tissue (12-18 m²) in humans ⁶. However, the primary cause of
66 poor brain deposition of therapeutics is often associated with an impermeable barrier termed
67 the blood-brain barrier (BBB), formed from brain microvascular endothelial cells and which
68 are highly selective in controlling the entry of endogenous and exogenous compounds into
69 the brain.

70 The development of CNS disorders is often associated with the process of oxidative stress
71 and leads to a range of neurological disorders such as epilepsy ⁷, Alzheimer's disease and
72 dementia ⁸. However, a novel category of potential therapeutic agents possessing anti-
73 oxidant activities are phytochemicals, which are derived from natural extracts from plants.
74 Over 8000 compounds have been identified as belonging to the general category of
75 polyphenols ⁹ of which flavonoids are a major class and contributing over 6500 distinct
76 compounds ¹⁰.

77 Many phytochemicals have been reported to possess CNS indicating effects including the
78 protection of neurons from neurotoxins and neuro-inflammation in degenerative diseases ¹¹⁻
79 ¹⁷. Furthermore, an increasing body of clinical evidence is supporting the view that
80 flavonoids impart a protective function towards dopamine neurons through the prevention of
81 oxidative damage and apoptosis ^{18,19}. The target site for flavonoids is thought to be
82 widespread within the CNS, but much attention has been focussed on the ability of
83 phytochemicals to interact with the GABA_A receptor, one of the most important
84 neurotransmitter sites within the CNS. Indeed, many phytochemicals demonstrated
85 significant inhibitory actions on GABA_A in low micromolar concentration, e.g. chrysin (3
86 μM) ²⁰ and 6-methylapigenin (495 nM) ²¹. Furthermore, chrysin has been demonstrated to
87 result in anxiolytic in mice at an intraperitoneal dose of 1 mg/kg ²². In addition to their action
88 on receptor sites, a range of phytochemicals have been demonstrated to modulate the genome
89 and proteome of the promiscuous network of membrane transporter proteins localised at the
90 BBB ²³.

91 Phytochemical flavonoids are therefore a potentially novel multi-faceted class of molecules
92 which show potential for a range of CNS patho-physiologies ²⁴⁻³⁶. However, many
93 phytochemicals are poorly soluble and are not immediately amenable to direct formulation
94 into dosage forms for oral/transdermal or parenteral systems.

95

96 Many groups have demonstrated successful loading and delivery of phytochemicals using
97 nanoparticle carrier systems to enhance their solubility and delivery, with the most commonly
98 studied phytochemical being curcumin³⁷⁻⁴⁰ and chrysin^{41, 42, 43}

99 A class of biocompatible nanomaterials that has gained attention for drug delivery are
100 mesoporous silica nanoparticles (MSNP). Silica is biocompatible and is often used in
101 inorganic nanoparticles^{44, 45}. Silica nanoparticles are highly porous in nature, with the pore
102 sizes, density and total surface area being highly tuneable making them excellent tools for
103 biomolecule detection, drug delivery systems and for contrast agent protectors⁴⁶⁻⁴⁸.
104 Mesoporous material was first discovered by Mobil Corporation in 1992⁴⁹ and termed
105 MCM-41, possessing a honeycomb-like porous structure with hundreds of pore channels
106 (termed mesopores) that have the potential to absorb molecules. This results in mesoporous
107 nanoparticles having a high surface area (> 900 m²/g), large pore volume (> 0.9 cm³/g) with
108 the added benefit of a tuneable pore size over a very narrow size distribution (2–10 nm)⁵⁰.
109 Furthermore, mesoporous silica nanoparticles have recently been used to demonstrate loading
110 and release of curcumin⁵¹.

111 To overcome the difficulties associated with crossing the BBB, approaches at bypassing the
112 BBB have more recently focused on exploiting the olfactory mucosa within the nasal cavity,
113 by virtue of the fact that olfactory neurones are directly exposed to the external environment
114^{52, 53} and provide a direct pathway to the olfactory bulb and brain. This region covers the
115 upper part of the nasal cavity with an approximate surface area of 2.5-10 cm² in humans⁵⁴.
116 It is primarily comprised of approximately 12 million olfactory receptor cells⁵⁵. The
117 olfactory region has been the focus of one of the major 'nose-to-brain' pathways to deliver
118 drugs directly to the brain through olfactory deposition. The first recorded success in the
119 delivery of a therapeutic agent into the brain in humans, following IN administration, was in
120 a patent application by William Frey II^{56, 57} reporting the successful delivery of neurological
121 agents and macromolecules (insulin)⁵⁸ targeting Alzheimer's disease. These reports
122 established a novel approach to target CNS drug delivery through potential bypassing of the
123 BBB, and is particularly attractive as the targeted delivery onto the olfactory mucosa (as
124 opposed to parenteral delivery) would require reduced drug loaded requirements.

125 Given the relative ease of preparation of MSNP and the tuneable nature of the nanomaterials,
126 MSNP are an interesting group of nanoparticles which have not fully been exploited for nose-
127 to-brain delivery. The aim of this study is to investigate the use of MSNP as carriers for the
128 poorly soluble phytochemicals curcumin and chrysin, which are known to possess CNS
129 pharmacological action⁵⁹⁻⁶⁸, and to assess their loading capacity and release profile along
130 with the cellular compatibility and *in-vitro* uptake into cultured olfactory cells.

131

132 **2. MATERIALS AND METHODS**

133 **2.1 Materials**

134 Dulbecco's Modified Eagle Medium (MEM), Dulbecco's Modified Medium: Nutrient
135 Mixture F12 (DMEM-F12), Dulbecco's Phosphate buffered saline (PBS), L-glutamine
136 200mM, non-essential amino acids (NEAA), penicillin/streptomycin and trypsin-EDTA
137 solution were obtained from PAA laboratories (Austria); foetal bovine serum (FBS) (Labtech,
138 Essex, UK); potassium chloride, magnesium sulphate, calcium chloride, acetonitrile,
139 orthophosphoric acid, acetic acid, ethanol, sodium hydroxide, and sodium chloride were
140 obtained from Fisher Scientific (Loughborough, UK); acutase (Biolegend, UK); gentamycin,
141 cetyl trimethylammonium bromide (CTAB), tetraethoxy orthosilicate (TEOS), (3-(4, 5-
142 dimethylthiazol-2-yl)-2, 5-diphenyl Tetrazolium bromide) MTT, trypan blue, dimethyl

143 sulfoxide (DMSO), potassium phosphate, ammonium hydroxide, rhodamine 6G, fluorescein
144 isothiocyanate (FITC), DAPI, collagen, cell culture water, monobasic were obtained from
145 Sigma-Aldrich (Dorset, UK).

146 **2.2 Methods**

147 **2.2.1 Preparation of MSNP**

148 MSNP were prepared using a modified method described by Fan et al ⁶⁹. Briefly, 1.0 g of
149 CTAB (2.74 mmol) was dissolved in 480 mL distilled water. Thereafter 3.5 mL of aqueous
150 sodium hydroxide solution (2 M) was added and the temperature of the mixture was raised to
151 80 °C. 5 mL TEOS (22.4 mmol) was then introduced drop wise into the reaction mixture
152 whilst stirring vigorously for two hours until a white precipitate was formed. The precipitate
153 was then filtered and washed with distilled water and methanol and dried under vacuum. The
154 surfactant template (CTAB) was removed by refluxing 1.5 g of the synthesized silica
155 particles with 1.5 mL of hydrochloric acid (37.2 % w/v) and 150 mL methanol for 6 hours.
156 The product was washed extensively with distilled water and methanol. The surfactant free
157 silica particles were placed under high vacuum with heating at 60°C to remove the remaining
158 solvent from the mesopores.

159 **2.2.2 Size and zeta-potential**

160 The size and zeta potential (ζ) of MSNPs were determined using dynamic light scattering
161 techniques through the use of a NanoBrook 90 Plus Zeta (Brookhaven Instruments
162 Corporation). 100 μ L of 1 mg/mL sonicated MSNPs suspension was added to 3 mL
163 ultrapure water, vortexed and used to measure the particles size. The mean diameter was
164 obtained from 3 runs of 3 minutes. The polydispersity index (PDI) was used to indicate the
165 particle size distribution within the sample. The zeta potential is an indicator for charge
166 present on the surface of nanoparticles, which is responsible for the stability of formulation
167 and interaction with cellular membranes. The zeta potential of nanoparticles is measured
168 using the principle of electrophoretic mobility under an electric field. The average of 3
169 readings (each reading = 30 runs) was reported. The temperature was maintained at 25°C
170 during the measurements.

171 **2.2.3 SEM**

172 Samples of MSNP were mounted on 12 mm aluminium pin stubs with 12 mm carbon tabs
173 and coated with 15nm of gold. The powders were imaged at 5 kV with a 150 pA beam in
174 high vacuum due to beam damage to the samples at higher kV's. The nanoparticles were
175 imaged at 10 kV with a 100 pA beam also in high vacuum using a Carl Zeiss EVO LS 15
176 with a Quorum QR105S gold coater.

177 **2.2.4 Nitrogen adsorption-desorption**

179 The specific surface areas of the blank MSNPs were analysed using the Brunauer–Emmet–
180 Teller (BET) method ⁷⁰ using a Quantchome NOVA (Quantchrom, Finland). The analysis
181 was based on the amount of Nitrogen (N₂) gas adsorbed at various partial pressures (P/P₀)
182 between 0.05 and 0.3. Before N₂ adsorption, samples were degassed under vacuum at a
183 temperature of 100° C. The nitrogen molecular cross sectional area (0.162 nm²) was used to
184 determine the surface area. The pore size distribution and total pore volume was determined
185 by using density functional theory (DFT) method. All calculations were software automated
186 (Quantchome NOVWIN, Quantchrom, Finland).

187

188 **2.2.5 TGA**

189 Thermal stability analysis of the functionalized silica was performed by thermogravimetric
190 analysis (TGA) using a Pyris 1 TGA (Perkin Elmer) instrument. 3 mg of MSNP materials
191 were analyzed under nitrogen purge with a starting temperature of 35 °C and 10 °C/min ramp
192 rate to 800 °C. The corresponding carbon, hydrogen and nitrogen elemental analysis was
193 performed using a LECO CHN-2000 elemental analyzer under flowing oxygen.

194 **2.2.6 DSC**

195 Heating curves of MSNP were obtained using differential scanning calorimeter (DSC Q200,
196 TA instruments, Delaware). Samples were weighed and 2-5 mg were loaded into a non-
197 hermetically crimped aluminium pan and heated under a nitrogen purge at the rate 50
198 mL/min. Samples were heated from 30 to 350°C at the heating rate 10°C/min under nitrogen.
199 Data was analysed using Universal Analysis 2000 software V4.5A TA instruments.

200 **2.2.7 FT-IR**

201 MSNP were further characterised by using FT-IR techniques for the bare MSNPs, and drug
202 loaded MSNPs. FT-IR absorbance was collected using a Nicolet iS5 FT-IR
203 spectrophotometer (Thermo Scientific,USA) over the spectral range of 550-4000 cm⁻¹.

204 **2.2.8 Phytochemical loading**

205 *Chrysin*: 20 mg/mL chrysin was dissolved in DMF and in a separate vial 20 mg/mL of
206 MSNPs were dispersed in DMF and bath sonicated for 15 minutes. A volume of 1 mL from
207 each vial was combined and resulted in a final concentration of 10 mg/mL of both chrysin
208 and MSNP. The glass vial was sealed and covered with foil, sonicated for 15 minutes in a
209 water sonicating bath and left for stirring at 100 rpm at room temperature. After 24 hours the
210 vial contents was filtered through a 0.22 µm cellulosic white membrane filter (MSI Micron
211 Separations Inc., USA). Chrysin loaded MSNP were termed 'Chry-MSNP'.

212 *Curcumin*: 20 mg/mL curcumin was dissolved in a 30:70 mixture acetone:ethanol and
213 processed as described above. Curcumin loaded MSNP were termed 'Curc-MSNP'.

214

215 The filtrate was collected to determine the loading (entrapment efficiency) and this approach
216 was termed the 'wet' approach. The entrapment efficiency (EE) was calculated based on the
217 following formula:

$$EE (\%) = \frac{\text{Compound added} - \text{Free "unentrapped compound"}}{\text{Compound added}} \times 100$$

218 where HPLC-UV methods were used to assess content.

219

220 The loaded nanoparticles collected on the filter paper were dried under high vacuum for 2
221 days, washed with PBS to remove superficially adsorbed phytochemicals and loading was
222 assessed through TGA. This approach was termed the 'dry' approach, where the loading
223 content (LC) was calculated from the difference between the final weight loss for MSNP and
224 phytochemical loaded MSNP at the end of the heating cycle and derived from data obtain
225 from TGA analysis.

226 Confirmation of phytochemical loading was further determined using HPLC-UV, DSC,
227 TGA, FT-IR and DLS/zeta potential analysis.

228 **2.2.9 Cellular toxicity towards olfactory cells: MTT assay**

229 To assess the compatibility between formulation and olfactory mucosa type cells, the porcine
230 olfactory bulb neuroblastoma cell line OBGF400 was used as an *in-vitro* cell culture model of
231 the olfactory cells/mucosa⁷¹. OBGF400 cells are bipolar to multipolar in nature with
232 prominent cell bodies and a distinctive nucleus and extending axonal structures confirm as
233 neuronal cells.

234 OBGF400 were a kind gift from Dr. Gail Scherba (University of Illinois, USA) and were
235 grown in DMEM/F-12 (Dulbecco's Modified Medium: Nutrient Mixture F12) supplemented
236 with sodium bicarbonate, HEPES, gentamicin (50 µg/mL), penicillin G/streptomycin, bovine
237 calf serum (BCS) in a humidified 37°C incubator with 5% CO₂. At 80-90 % confluency, the
238 media was aspirated and cells were treated with Acutase[®] for 20-30 minutes prior to
239 passaging.

240 Cells were seeded into 96-well plates at a density of 1x10⁴ cells per well. Cells were
241 subsequently exposed to 10-1000 µg/mL MSNPs for 24 hours at 37 °C and 5 % CO₂
242 humidified environment and cellular toxicity was assessed using a 3-(4,5-Dimethylthiazol-2-
243 yl)-2,5-Diphenyltetrazolium Bromide (MTT) assay. Briefly, following incubation the media
244 was removed and replaced with 100 µL of media containing 0.5 mg/mL MTT dissolved in
245 PBS and incubated at 37 °C in an air humidified environment for 4 hours. Thereafter, the
246 media was removed and 100 µL of DMSO was added and the plates left to incubate for 15
247 minutes in the dark. The UV-absorbance of the formazan product was determined at 595 nm.

248 The UV-absorbance of the formazan product was measured on a multi-plate reader (Bio-Rad
249 laboratories, Hercules, CA) using 570 nm as a test wavelength and 600 nm as a reference
250 wavelength. The mean of the blank UV-absorbance was subtracted from the UV-absorbance
251 of each controls and samples and percentage viability was calculated as follows:

$$252 \quad \% \text{ cell viability} = \frac{\text{absorbance of sample}}{\text{absorbance of control}} * 100$$

253

254 The cellular viability IC₅₀ was subsequently calculated using a sigmoidal dose response
255 function. Each concentration was assayed in eight wells and run in three independent
256 experiments and results expressed as percentage cytotoxicity relative to a control (0.5%
257 DMSO).

258 The cellular toxicity of curcumin and chrysin were also assessed using OBGF 400 cells at a
259 concentration range of 0.01-50,000 µM, as described above. The cell viability was calculated
260 by comparing the absorbance of phytochemical or drug treated well to that of control well.

261 **2.2.10 Cellular toxicity towards olfactory cells: Live cell imaging**

262 To assess the morphological alterations in cellular structures when exposed to MSNP, Curc-
263 MSNP and Chry-MSNP, live cell imaging of OBGF400 was conducted over a 40-hour period
264 in an oxygen, CO₂ and humidity controlled phase contrast imaging systems (CellIQ[®], Chip-
265 Man Technologies, Tampere, Finland). OBGF400 cells were seeded into wells of a 6-well
266 plate at a density of 5x10⁵ cells/well and allowed to adhere and proliferate to 70 %
267 confluence. Subsequently wells were washed with warm HEPES (25 mM) buffered HBSS,
268 followed by the addition of 50-150 µg/mL of MSNP, Curc-MSNP and Chry-MSNP dispersed

269 in maintenance media for 40 hours with images captured within a defined window within
270 each well every 15 minutes using live-cell imaging and presented as images.

271 **2.2.11 Cellular uptake of nanoparticles into olfactory cells**

272 Coverslips were sterilised in 70% ethanol for 30 minutes, dried in a laminar air hood and
273 coated with $6 \mu\text{g}/\text{cm}^2$ of a collagen prepared in sterile water from a 0.1 % w/v (0.1 M acetic
274 acid) stock solution, with coating taking place in 12-well plates. Plates were left to dry in the
275 laminar air flow for 2 hours. Excess collagen was then removed and coverslips washed with
276 sterile water and left for drying. Thereafter cell suspensions of OBGF 400 cells were seeded
277 at a density of 1×10^5 cells/ cm^2 into wells of a 12 well plate containing the coated coverslips
278 and left to adhere and proliferate to a confluency of approximately 70% in a 5% CO_2
279 humidified incubator.

280 To identify the optimal particle size range for olfactory uptake, fluorescent latex beads
281 (carboxylate modified) of 100 nm ($\lambda_{\text{ex}} \sim 491$ nm; $\lambda_{\text{em}} \sim 521$ nm) and 500 nm ($\lambda_{\text{ex}} \sim 575$ nm;
282 $\lambda_{\text{em}} \sim 610$ nm) were initially utilised as a rapid fluorescence-based screening tool to consider
283 the boundary range of 100-500 nm for nanoparticle uptake into OBGF400 cells. Fluorescent
284 latex beads were dispersed into HEPES (25mM) buffered HBSS at a concentration of 0.1 %
285 v/v and sonicated for 10 minutes in a water-bath sonicator prior to the addition into wells.
286 Subsequently, to assess the cellular uptake of formulated MSNP (section 2.2.1), FITC was
287 passively loaded into MSNP (see supplementary materials section 1), dispersed into HEPES
288 (25mM) buffered HBSS at a concentration of 0.1 % v/v and sonicated for 10 minutes in a
289 water-bath sonicator prior to the addition into wells

290 Coverslips were incubated for 2 hours in a 5 % CO_2 humidified incubator before being
291 washed with ice cold HEPES (25mM) buffered HBSS and fixed with 4 % w/v
292 paraformaldehyde for 30 minutes in the dark. The coverslips were then mounted onto glass
293 slides with mounting media containing 4',6-diamidino-2-phenylindole (DAPI). The
294 localisation of the latex beads was analysed using an upright confocal microscope (Leica SP5
295 TCS II MP) and visualised with a 40x oil immersion objective. All images were acquired
296 using an argon laser at 494 nm or DPSS 561 laser at 561 nm to visualise beads/MSNP and a
297 helium laser to visualise DAPI at 461 nm.

298 **2.2.12 HPLC detection of phytochemicals**

299 The detection of curcumin was based on an adapted method previously reported by Li et al ⁷².
300 An Agilent 1200 Series (Waldbronn, Germany) equipped with a multiple wavelength detector
301 (MWD) and a Phenomenex Luna C18 (150×4.6 mm) 5 μm column was used for RP-HPLC.
302 The mobile phase was prepared using ACN:5% acetic acid in a ratio of 45: 55 (v/v). Mobile
303 phases were filtered through a 0.45 μm filter and sonicated before use. The flow rate was
304 maintained at 0.8 mL/min with a 15 minutes run time and injection volume of 20 μL , while
305 column temperature was mainlined at ambient temperatures. Calibration curves were
306 constructed using standard solutions of known concentrations from 5 to 50 $\mu\text{g}/\text{mL}$. The
307 software used for data collection, analysis and control of the system was ChemStation
308 Version 1.24 SP1. The UV detection of curcumin was measured at 420 nm.

309 An RP-HPLC method was used to quantify chrysin ⁷³. The same HPLC system described
310 above was used to analyse chrysin samples. The mobile phase comprised of
311 water:methanol:acetonitrile:phosphoric acid in a ratio of 60:30:38:1 (v/v). Mobile phases
312 were filtered through 0.45 μm filter and sonicated before use. The flow rate was maintained
313 at 1.0 mL/min with 17 minutes run time and the injection volume was 10 μL while column
314 temperature was kept at ambient temperatures. Calibration curves were constructed using

315 standard solutions of known concentrations from 0.78 to 10,000 $\mu\text{g/mL}$. The UV detection of
316 chrysin was measured at 262 nm.

317

318 **2.2.13 Release of phytochemicals from MSNP**

319 To assess the *in-vitro* release of curcumin and chrysin from MSNPs, studies were performed
320 in phosphate buffered saline (154 mM PBS pH 7.4) containing 0.1 % Tween 80.

321 Phytochemical loaded MSNP, 2 mg, were dispersed into 2 mL of release medium, briefly
322 sonicated and placed in a shaking incubator maintained at 37 °C and 100 rpm. Samples were
323 withdrawn at set time intervals and the volume replaced with an equal volume of pre-warmed
324 release medium. The release of phytochemicals was assessed through HPLC-UV methods.

325 Throughout the release studies Tween 80 was used to maintain the sink conditions and also to
326 dissolve curcumin in the release medium⁷⁴. The results were calculated in terms of
327 cumulative release (% w/w) relative to actual entrapped weight of curcumin or chrysin in the
328 MSNPs. To assess the impact of pH on drug release, release studies were also conducted at
329 pH 5.5 (average nasal pH).

330 **2.2.14 Statistical analysis**

331 Unless otherwise stated, three independent experiments were carried out for each study.
332 Statistical significance was evaluated by one-way ANOVA or paired two-tail Students t-test
333 using GraphPad Prism version 6.00 (GraphPad Software, La Jolla California USA,
334 www.graphpad.com). Unless otherwise stated, data is reported as mean \pm standard deviation
335 (SD). A significance level (P-value) of < 0.05 was considered as statistically significant.

336

337 **3. RESULTS AND DISCUSSION**

338 **3.1 MSNP formulation and characterisation**

339 MSNP were formulated according to the methods described by Fan et al⁶⁹, which employs a
340 templating approach where template removal determines the hollow interior of the MSNP.
341 During the formation CTAB is responsible for the formation of the shell and TEOS
342 determines the hollow interior of the MSNPs⁷⁵.

343 Synthesis of MSN yielded particle sizes of 216.5 ± 2.1 nm with a PDI of 0.13 ± 0.02 and a
344 zeta-potential of -23.9 ± 0.4 (Figure 1A), similar to that reported by Fan et al (180-185 nm). To
345 confirm the particle size of the formulated MSNP, SEM imaging was used to assess the
346 morphological structure of MSNP. The nanoparticles developed demonstrated a uniform
347 particle distribution of similar sizes and relatively uniform smooth particles and particle sizes
348 of approximately 200 nm (Figure 1B and 1C).

349 FT-IR assessment was also used to assess the removal of the template from the mesoporous
350 materials and confirmed with four bands at 550, 1500, 2900 and 3000 cm^{-1} before CTAB
351 removal (Figure 2) corresponding to the CH_2 and CH_3 groups in CTAB molecule structure,
352 which were eliminated after template removal (Figure 2).

353 To determine the porosity of the MSNP and ascertain the pore volume and density, nitrogen
354 adsorption/desorption isotherms were generated. The nitrogen absorption-desorption
355 isotherms identify the characterise hysteresis-type loop associated with capillary (pore)
356 condensation at $P/P_0 > \approx 0.2$ (Figure 3A). The hysteresis loop can be classified as a H1 loop,
357 which is often associated with porous materials exhibiting a narrow distribution of relatively
358 uniform (cylindrical-like) pores. The overall distribution of the pore radius was confirmed

359 through BJH analysis and demonstrated a narrow pore radius relative to the cumulative pore
360 volume with the majority of the radius distribution, $dV(r)$, located <20-30 Ang (< 10 nm).
361 Furthermore, the pore width distribution confirmed a pore with distribution of < 4 nm (Figure
362 3B and C) with a large surface area $987.67 \pm 3.38 \text{ m}^2/\text{g}$ and the DFT method confirms that
363 the average pore size of $1.93 \pm 0.01 \text{ nm}$ (Figure 3B and C) with total pore volume $0.95 \pm$
364 0.004 cc/g and possessing similar porosity to other reported MSNP^{76,77}.

365 3.2 Phytochemical loading into MSNP

366 The loading of curcumin into MSNP was confirmed through FT-IR analysis. The
367 characteristic IR absorption frequencies in the spectral range of $550\text{-}4000 \text{ cm}^{-1}$ were
368 measured for free curcumin and Curc-MSNPs. The interaction between MSNPs and
369 curcumin after being loading was also analysed using FTIR. Curcumin spectra shows the
370 following characteristic peaks: broad peak at 3420 cm^{-1} confirming the intermolecular
371 hydrogen bonding in isolated silanol and enolic hydroxyl groups, with a broader shift when
372 incorporated into MSNP indicating potential enhancement of hydrogen bonding (Figure 4A).
373 The signature peaks of curcumin are located at 1627 cm^{-1} and 1602 cm^{-1} and are attributed to
374 the C=C double bonds and aromatic C=C double bonds, respectively⁷⁸ (Figure 4B). Finally
375 bands at $1,279 \text{ cm}^{-1}$ and $1,152 \text{ cm}^{-1}$ were assigned to the aromatic C-O stretching and
376 stretching in the C-O-C⁷⁸ (Figure 4B)^{79,80}. In all cases, these bands were absent in the blank
377 MSNP. For chrysin, the FT-IR spectrum shows bands at 2921 cm^{-1} , 2710 cm^{-1} and 2631
378 cm^{-1} for stretching in the C-H and C=C (Figure 4C and D). Furthermore, carbonyl group
379 vibrations coupled with the double band in the γ -benzopyrone ring at 1653 cm^{-1} and
380 absorption bands at 1612 , 1577 and 1450 cm^{-1} related to carbon vibration in benzene and γ -
381 pyrone rings (valance vibrations C=C) can be observed (Figure 4D)⁸¹.

382 To further characterise the loading of phytochemicals into MSNP, DSC thermographs were
383 analysed for blank and loaded MSNP. The thermograms of pure curcumin and chrysin show
384 characteristic single melting endothermic peak at 176°C (Figure 5A) and 286°C respectively
385 (Figure 5B), which were absent in the loaded MSNP (Figure 5A). Furthermore, the absence
386 of characteristic single melting endothermic peaks for loaded MSNP confirms the washing
387 step in the 'dry method' had removed residual phytochemical adsorbed onto the surface of
388 the MSNPs and secondly that the loaded phytochemical was present in the amorphous form.

389 Furthermore, TGA analysis show that the total weight loss of the loaded MSNP at the end of
390 the run was $22.16 \pm 1.12 \%$ compared to the blank MSNPs, $7.21 \pm 0.45 \%$ with a calculated
391 LC of $14.95 \pm 0.67 \%$ and which corresponds to the calculated EE of $12.34 \pm 1.28 \%$ for the
392 'wet method' for curcumin (Figure 5C). For chrysin the total weight loss of the Fan-MSNP
393 at the end of the run was $21.07 \pm 0.75 \%$ compared to the blank MSNPs, $9.58 \pm 1.94 \%$ with a
394 calculated LC of $11.49 \pm 1.19 \%$ and which corresponds to the calculated EE of 12.34 ± 1.28
395 $\%$ for the 'wet method' (Figure 5D).

396 To confirm loading of curcumin into MSNP, particle size demonstrating an increase in the
397 hydrodynamic mean diameter from $216.8 \pm 2.1 \text{ nm}$ to $263.51 \pm 8.3 \text{ nm}$ after loading with
398 curcumin ($P \leq 0.01$) with a statistically significant increase in the PDI from 0.13 ± 0.02 to
399 0.26 ± 0.05 ($P \leq 0.05$) (Figure 6A). Furthermore the zeta potential of the Curc-MSNP
400 decreased from $-23.9 \pm 0.4 \text{ mV}$ to $-16.9 \pm 0.9 \text{ mV}$ ($P \leq 0.01$) (Figure 6B). This increase in
401 particle size and PDI has been previously reported after loading curcumin in their
402 mesoporous nanoparticles^{51,79}. Furthermore the decrease in zeta potential following loading
403 has previously been reported, however the polarity of the resultant charge is a function of the
404 pH of the media that the zeta potential is measured in, with reports that a lower pH media
405 often leads to more positive zeta potential with loading⁸²⁻⁸⁵.

406 Similarly for chrysin the hydrodynamic mean diameter increased from 216.8 ± 2.1 nm to
407 283.5 ± 8.3 nm after loading ($P \leq 0.01$) with a statistically significant increase in the PDI
408 from 0.13 ± 0.02 to 0.31 ± 0.11 ($P \leq 0.05$) (Figure 6C) and an associated decrease in zeta
409 potential from -23.9 ± 0.4 mV to -30.8 ± 0.3 mV ($P \leq 0.01$) (Figure 6D). However reports
410 from other chrysin loaded nanoparticle systems indicate a negative zeta potential in the range
411 we detected^{86,87}.

412 Traditionally the zeta potential has been considered an important element for cellular
413 interaction, with positively charged NP being favoured over negatively charged NP due to the
414 negative charge of a cell membrane⁸⁸. That said, a number of reports have identified that the
415 zeta potential is less of an issue for MSNP due to their highly mesoporous nature^{89,90}.
416 Furthermore the endosome escaping, “proton sponge” effect⁹¹, may explain the ability of
417 Fan-MSNP to undergo internalisation, considering negative charge, without any specific
418 ligands for receptor mediated endocytosis.

419 With TGA analysis some weight loss at low temperature may have been attributed to
420 adsorbed water whereas the weight loss at higher temperatures can be attributed to loss of
421 surface silanol groups. However, no significant weight loss was evident during the study and
422 this implies Fan-MSNP were thermally stable⁹². In the case of both chrysin and curcumin,
423 the loaded nanoparticles demonstrated no characteristic melting point depression confirming
424 the amorphous nature of the loaded phytochemical and confirming negligible drug adsorbed
425⁹³.

426 **3.3 Cellular toxicity towards olfactory cells**

427 To investigate the toxicity of MSNP, curcumin and chrysin towards OBG400 cells a cell
428 viability assay was conducted with phytochemicals/MSNP exposed to OBG400 for 24
429 hours. For MSNP, cell viability was generally maintained across the concentration range of
430 10-100 $\mu\text{g/mL}$ (Figure 7A), with a statistically significant ($P \leq 0.01$) decrease in viability from
431 100 $\mu\text{g/mL}$ onwards. For curcumin (Figure 7B) and chrysin (Figure 7C), cell viability was
432 maintained across the concentration range of 0.001-10 μM and an IC_{50} of 33 ± 0.18 μM was
433 determined for curcumin. For chrysin at 100 μM , a statistically significant ($P \leq 0.01$)
434 decrease in cell viability was observed (to 58.2 ± 8.5 %). Reports of toxicity of MSNP with
435 olfactory cells have not been reported by others but contradictory reports comment on
436 relationships between the particle size and cellular toxicity, which appears to be cell line
437 specific. For example, smaller-sized silica nanoparticles induced severe cellular damage in
438 lung cancer cells, myocardial cells, and human endothelial cells⁹⁴⁻⁹⁶ and this was thought to
439 be related to the fact that smaller nanoparticles have larger ratio of surface area to weight and
440 therefore potentially more contact with the cells to induce damage⁹⁷⁻⁹⁹. However others have
441 reported that larger silica nanoparticles are more cytotoxic than smaller particles on human
442 hepatoma cells¹⁰⁰.

443 All MTT assays were conducted in cell culture media containing serum. A possible
444 explanation for the conflicting reports in cellular toxicity associated with MSNP (and NP
445 more generally) may be associated with a protein corona that is formed on the surface of
446 silica nanoparticles that may alter the cytotoxic potential of the nanoparticles when in contact
447 with serum proteins from tissue culture media^{101,102}.

448 No other reports are available of the cellular toxicity of curcumin or chrysin with OBG400
449 cells, however others have reported similar IC_{50} in CNS related cell lines (porcine brain
450 microvascular endothelial cells PBMEC/C1-2: 63 ± 1.2 μM)²³. Similar IC_{50} values have been
451 reported for curcumin, 15.2 μM and 16.4 μM against A2780CP and MDA-MB-231 cells

452 respectively⁷⁴. Mukerjee and Vishwanatha¹⁰³ found the IC₅₀ of curcumin loaded PLGA
453 nanoparticle was 31µM for PWR 1E cells as compared to 37µM of free curcumin

454 Any foreign particle to be taken up by the cell is dependent upon many factors such as size,
455 charge, affinity etc. It has been reported that nanoparticles smaller than 100 nm could cause
456 unspecific cellular uptake and cytotoxicity¹⁰⁴. Silica nanoparticles in the size range of 50-300
457 nm are capable of inducing endocytosis¹⁰⁵ without causing any cytotoxicity and they have
458 been reported to possess high affinity to many phospholipids present on the surface of the
459 cell, which may even induce pinocytosis¹⁰⁶.

460 To assess the morphological alteration of cellular structures when exposed to MSNP, Curc-
461 MSNP and Chry-MSNP, a gas and humidity controlled phase contrast imaging study was
462 conducted using the CellIQ[®] imaging system. OBGF400 cells, grown in wells of a 6-well
463 plates, were exposed to 50-150 µg/mL of MSNP, Curc-MSNP and Chry-MSNP for 40 hours
464 with images captures within a defined window within each well every 15 minutes using live-
465 cell imaging. The impact of MSNP on cell viability/proliferation at 150 µL/mL demonstrate
466 a clear impact on the viability and proliferation of OBGF400 over 40 hours resulting in a
467 reduction in the cell morphological volume and cell death. This effect was diminished at a
468 concentration of 50 µg/mL, where cell morphology was maintained throughout the
469 incubation period (See supplementary materials figure 2)

470 With Chry-MSNP, a similar impact on cell viability was noted at 150 µg/mL. However, at 50
471 µg/mL cell morphology was seen to change associated with the apoptosis of some cells (See
472 supplementary materials figure 3). For Curc-MSNP, cell morphology was noted to alter at
473 150 µg/mL leading to an increase in cell death over time, however at 50 µg/mL cell viability
474 was not affected and proliferation of cells was noted (See supplementary materials figure 4).

475 **3.4 Cellular uptake of nanoparticles into olfactory cells**

476 A key goal for our studies was to demonstrate uptake of MSNP into olfactory bulb neuronal
477 cells. To assess this process fluorescent latex beads of 100 nm and 500 nm size ranges were
478 selected to allow cellular imaging of the intracellular localisation of beads, providing some
479 insight into appropriate size ranges for viable cellular uptake. For 100 nm sized latex beads
480 the cellular localisation of the beads is evident, particularly in the membrane regions and
481 cytoplasm (Figure 8). For the 500 nm sized latex beads a x63 magnification was used to
482 enlarge isolated OBGF400 cells with membrane localisation and partial cytoplasmic trapping
483 observed (Figure 8).

484 The fluorescent molecule FITC was subsequently passively loaded into MSNP resulting in an
485 EE of 48 ± 2.3 % and the release of FITC was assessed in PBS (pH 7.4) media (See
486 supplementary materials). The duration of the release study was set at 2 hours, primarily as a
487 result of the short exposure-time expected with nasally delivered formulation coupled with
488 the limited duration with which cell cultures can proliferate in the absence of growth media.
489 Minimal FITC was identified as having been released from FITC-MSNP, 4.8 ± 0.19 %, over
490 a 2-hour period suggesting the relative stability of the FITC molecule within the MSNP
491 structure (see supplementary materials Figure 1).

492 To further discern the exact localisation of MSNP within the cell, FITC loaded MSNP were
493 prepared and incubated with OBGF400 cells before z-stack confocal microscopy was used to
494 capture FITC- MSNP fluorescence through the z-dimension of the cell The confocal stage
495 was set at the upper-most boundary of the OBGF 400 cells and the stage moved down
496 towards the coverslip with images captured over a z-dimension of approximately 5 µm. At
497 the onset of the z-stack analysis, FITC-MSNP is localised on the exterior of the cell boundary

498 and potentially on the surface of the cells (10763 μm). As the stage progresses, the
499 localisation of FITC-MSNP increases with clear demarked zones of cytoplasmic localisation
500 near the ‘mid-to-bottom’ regions of the cells (Figure 9).

501 However, cellular uptake of both sizes of beads were detected using confocal microscopy and
502 suggest MSNP formulation over this size range would be appropriate for olfactory uptake.
503 Although the use of fluorescent latex beads as retrograde transport markers for neuronal
504 pathways is not new¹⁰⁷⁻¹⁰⁹, the application to olfactory bulb neuronal cells is novel indicates
505 the potential for nano-sized material to penetrate into this class of cells.

506 MSNP possessing a negative zeta potential have been previously reported¹¹⁰⁻¹¹² and
507 associated with successful cellular uptake for both naïve MSNP and modified MSNP. The
508 uptake of MSNP in our study is presumed to be through a nonspecific pathway as the use of
509 naïve MSNP incorporated no surface functionalisation for cellular targeting. Furthermore,
510 the location of clarithin coated vesicles on olfactory and the reported uptake of MSNP via
511 clathrin-dependent endocytotic pathways due to their siliceous composition, and unique
512 hexagonal exterior and internal hexagonal mesopores¹¹³ would indicated this would be the
513 favoured uptake route of otherwise electronically unfavourable interactions between MSNP
514 and the cell membrane. Furthermore, the it has been reported that nanoparticles possess a
515 negative zeta potential illicit a “proton sponge” effect within the endosome whereby the
516 negative zeta potential MSNP would aid in buffering the internal charge of the endosome,
517 resulting in an increase in osmotic pressure (due to Cl⁻ influx) and swelling and finally
518 facilitating endosomal escape through rupturing⁹¹.

519

520 **3.5 Phytochemical release study from the mesoporous silica nanoparticles**

521 The release of curcumin from Curc-MSNP was assessed over 24 hours and demonstrated a
522 pH sensitive release phenomena. A burst effect was also evident after 1 hour with 12 % and
523 16.6 % released at pH 7.4 and pH 5.5 respectively (Figure 10A). Release at pH 7.4 was
524 slower than that at pH 5.5, with 16.1 ± 1.6 % released at 24 hours ($P \leq 0.001$). At pH 5.5
525 release increased over 24 hours to 53.2 ± 2.2 % ($P \leq 0.001$). However, no significant
526 increase in curcumin release was observed from 1 hour to 24 hours.

527 The release of chrysin from Chry-MSNP was assessed over 24 hours and also demonstrated a
528 pH sensitive release phenomena. A burst effect was evident after 1 hour with 3.2 ± 1.2 % and
529 7.1 ± 1.6 % released at pH 7.4 and pH 5.5 respectively (Figure 10B). Release at pH 5.5 was
530 slower than that for pH 7.4 ($P \leq 0.001$), with 9.4 ± 0.6 % and 16.8 ± 0.8 % at 24 hours
531 respectively. However statistically significant differences ($P \leq 0.001$) were also observed
532 between 1 hour and 24 hours release at each pH studied. Furthermore, the release profile for
533 both phytochemicals demonstrated a burst effect at early time points and this pattern has also
534 been reported elsewhere¹¹⁴⁻¹¹⁷. This may be a result of the rapid dissolution of the loaded
535 phytochemicals closer to the exterior of the pores with slower penetration of solvent into the
536 pores as a result of the micro/meso size pores of < 2 nm .

537 The differences in release of curcumin from mesoporous nanoparticles at difference pHs is
538 important as the release in the nasal cavity (pH 5.5) is likely to be more rapid. Furthermore,
539 it has been reported that curcumin is relatively unstable at pH 7.4 compared to more acidic
540 pH, which may explain the lack of increase in cumulative release from 1 hour to 24 hours
541 (~ 1.8 %) compared to the $\sim 36\%$ increase in cumulative release at pH 5.5 at 24 hours¹¹⁷⁻¹¹⁹.

542 The degradation has been reported to be complex but at a pH < 1, curcumin exists in the
543 protonated form (H_4A^+), with increasing pH the neutral form (H_3A) predominates.
544 Furthermore stability in acidic conditions is likely due to its conjugated diene structure which
545 becomes gradually destroyed as the proton is removed during the dissociation of the phenolic
546 groups within the structure of curcumin (H_2A^- , HA^{2-} and A^{3-}) which occurs at higher pHs
547 and is likely the cause of curcumin being significantly more prone to degradation^{120, 118}. An
548 analysis of the HPLC chromatograms for curcumin at 1 hour and 24 hour also confirms
549 differences in peak ratios suggesting degradation of curcumin at pH 7.4 rather than pH 5.5
550 (See supplementary materials figure 5).

551 Therefore at nasal pH (~5.5) both curcumin and chrysin loaded MSNP would be expected to
552 be relatively stable at physiological pH and undergo release from the MSNP.

553 The difference in cumulative release between phytochemicals may be related to the pore size.
554 The pore size influences the potential loading capacity (and therefore potentially the release
555 pattern) from MSNP^{106,121}. Furthermore, the penetration of the phytochemicals within the
556 naïve (non-functionalised) pores of MSNP would largely therefore depend on the molecular
557 properties of the loaded phytochemicals.

558 Curcumin possesses a larger molecular weight (368.38 g/mol) and 3 distinct molecular entities:
559 two aromatic ring systems containing o-methoxy phenolic groups, connected with a seven
560 carbon linker consisting of an α,β -unsaturated β -diketone structure with the diketo group
561 exhibiting keto-enol tautomerism. Chrysin (254.23 g/mol) on the other hand belongs to the
562 flavone group of phytochemicals and consists of A and C rings, and a phenyl B ring attached
563 to position 2 of the C ring, thus essentially three pi-pi conjugated rings. As a result of the
564 narrow pore width, the difference in release rates may be a function of the ability of curcumin
565 to diffuse from within the porous structure more rapidly (due to steric hindrances) compared
566 to chrysin. Furthermore chrysin possesses planar stereochemistry and the pi-pi structure would
567 enhance the non-covalent bonding interactions within the pores, resulting in a slower release
568 profile.

569

570 **4. CONCLUSION**

571 Age related neurological disorders such as Parkinson's disease (PD) and Alzheimer's disease
572 (AD), are insidious progressive neurological disorders which are expected to increase in
573 incidence over the next century. Current approaches to CNS drug delivery are often
574 hampered by poor targeting and drug delivery to the BBB and nose-to-brain delivery,
575 following olfactory targeting, provides a promising novel way to bypass the BBB.

576 We have developed phytochemical-loaded MSNP and have systemically investigated the
577 loading, uptake and *in-vitro* release of phytochemicals from MSNP. Our studies have
578 demonstrated that nanoparticles below 500 nm would be capable of being taken up by
579 olfactory cells and that the release of phytochemicals from MSNP is pH dependant,
580 potentially suited to the slightly acidic nature of the nasal cavity.

581 Although the successful intranasal delivery of the formulation onto the olfactory mucosa may
582 significantly enhance its eventual delivery to the brain, we believe that the present study
583 demonstrates the benefits of MSNP as a drug carrier and particularly in its applications
584 towards nose-to-brain delivery of phytochemical loaded nano-carriers.

585

586 **ACKNOWLEDGMENTS**

587 The authors would like to thank Aston University for providing the Overseas Student Scholar
588 Scheme to fund this project. We would also like to acknowledge Aston Research Centre for
589 Healthy Ageing and Charlotte Bland for assisting with the collection of confocal imaging
590 data.

591

592 **REFERENCES**

593

- 594 1. WHO, *Neurological Disorders: Public Health Challenges*. World Health
595 Organization: 2006.
- 596 2. Kola, I.; Landis, J. Can the pharmaceutical industry reduce attrition rates? *Nat Rev*
597 *Drug Discov* **2004**, *3*, (8), 711-5.
- 598 3. Pardridge, W. M. The blood-brain barrier: bottleneck in brain drug development.
599 *NeuroRx* **2005**, *2*, (1), 3-14.
- 600 4. Lipinski, C. A. Drug-like properties and the causes of poor solubility and poor
601 permeability. *J Pharmacol Toxicol Methods* **2000**, *44*, (1), 235-49.
- 602 5. Pardridge, W. M. CNS drug design based on principles of blood-brain barrier
603 transport. *Journal of neurochemistry* **1998**, *70*, (5), 1781-92.
- 604 6. Abbott, N. J.; Romero, I. A. Transporting therapeutics across the blood-brain barrier.
605 *Molecular Medicine Today* **1996**, *2*, (3), 106-113.
- 606 7. Diniz, T. C.; Silva, J. C.; de Lima-Saraiva, S. R.; Ribeiro, F. P.; Pacheco, A. G.; de
607 Freitas, R. M.; Quintans-Junior, L. J.; Quintans Jde, S.; Mendes, R. L.; Almeida, J. R. The
608 role of flavonoids on oxidative stress in epilepsy. *Oxid Med Cell Longev* **2015**, *2015*, 171756.
- 609 8. Bennett, S.; Grant, M. M.; Aldred, S. Oxidative stress in vascular dementia and
610 Alzheimer's disease: a common pathology. *Journal of Alzheimer's disease : JAD* **2009**, *17*,
611 (2), 245-57.
- 612 9. Pandey, K. B.; Rizvi, S. I. Plant polyphenols as dietary antioxidants in human health
613 and disease. *Oxid Med Cell Longev* **2009**, *2*, (5), 270-278.
- 614 10. Kong, Y.; Ma, W.; Liu, X.; Zu, Y. G.; Fu, Y. J.; Wu, N.; Liang, L.; Yao, L. P.;
615 Efferth, T. Cytotoxic Activity of Curcumin towards CCRF-CEM Leukemia Cells and Its
616 Effect on DNA Damage. *Molecules (Basel, Switzerland)* **2009**, *14*, (12), 5328-5338.
- 617 11. Williams, R. J.; Spencer, J. P. Flavonoids, cognition, and dementia: actions,
618 mechanisms, and potential therapeutic utility for Alzheimer disease. *Free Radic Biol Med*
619 **2012**, *52*, (1), 35-45.
- 620 12. Solanki, I.; Parihar, P.; Mansuri, M. L.; Parihar, M. S. Flavonoid-based therapies in
621 the early management of neurodegenerative diseases. *Adv Nutr* **2015**, *6*, (1), 64-72.
- 622 13. Shukitt-Hale, B. Blueberries and neuronal aging. *Gerontology* **2012**, *58*, (6), 518-23.
- 623 14. Mecocci, P.; Tinarelli, C.; Schulz, R. J.; Polidori, M. C. Nutraceuticals in cognitive
624 impairment and Alzheimer's disease. *Front Pharmacol* **2014**, *5*, 147.
- 625 15. Macready, A. L.; Kennedy, O. B.; Ellis, J. A.; Williams, C. M.; Spencer, J. P.; Butler,
626 L. T. Flavonoids and cognitive function: a review of human randomized controlled trial
627 studies and recommendations for future studies. *Genes Nutr* **2009**, *4*, (4), 227-42.
- 628 16. Cherniack, E. P. A berry thought-provoking idea: the potential role of plant
629 polyphenols in the treatment of age-related cognitive disorders. *Br J Nutr* **2012**, *108*, (5), 794-
630 800.

- 631 17. Blumberg, J. B.; Ding, E. L.; Dixon, R.; Pasinetti, G. M.; Villarreal, F. The science of
632 cocoa flavanols: bioavailability, emerging evidence, and proposed mechanisms. *Adv Nutr*
633 **2014**, *5*, (5), 547-9.
- 634 18. Mercer, L. D.; Kelly, B. L.; Horne, M. K.; Beart, P. M. Dietary polyphenols protect
635 dopamine neurons from oxidative insults and apoptosis: investigations in primary rat
636 mesencephalic cultures. *Biochem Pharmacol* **2005**, *69*, (2), 339-45.
- 637 19. Meng, X.; Munishkina, L. A.; Fink, A. L.; Uversky, V. N. Molecular mechanisms
638 underlying the flavonoid-induced inhibition of alpha-synuclein fibrillation. *Biochemistry*
639 **2009**, *48*, (34), 8206-24.
- 640 20. Medina, J. H.; Paladini, A. C.; Wolfman, C.; de Stein, M. L.; Calvo, D.; Diaz, L. E.;
641 Peña, C. Chrysin (5,7-di-OH-flavone), a naturally-occurring ligand for benzodiazepine
642 receptors, with anticonvulsant properties. *Biochemical Pharmacology* **1990**, *40*, (10), 2227-
643 2231.
- 644 21. Wasowski, C.; Marder, M.; Viola, H.; Medina, J. H.; Paladini, A. C. Isolation and
645 identification of 6-methylapigenin, a competitive ligand for the brain GABA(A) receptors,
646 from *Valeriana wallichii*. *Planta medica* **2002**, *68*, (10), 934-6.
- 647 22. Wolfman, C.; Viola, H.; Paladini, A.; Dajas, F.; Medina, J. H. Possible anxiolytic
648 effects of chrysin, a central benzodiazepine receptor ligand isolated from *Passiflora coerulea*.
649 *Pharmacology, biochemistry, and behavior* **1994**, *47*, (1), 1-4.
- 650 23. Kaur, M. Phytochemical Mediated Modulation Of Breast Cancer Resistance Protein
651 At The Blood Brain Barrier And Blood Cerebrospinal Fluid Barrier. Aston University, 2016.
- 652 24. Katayama, K.; Masuyama, K.; Yoshioka, S.; Hasegawa, H.; Mitsunashi, J.; Sugimoto,
653 Y. Flavonoids inhibit breast cancer resistance protein-mediated drug resistance: transporter
654 specificity and structure-activity relationship. *Cancer Chemother Pharmacol* **2007**, *60*, (6),
655 789-97.
- 656 25. Breedveld, P.; Beijnen, J. H.; Schellens, J. H. M. Use of P-glycoprotein and BCRP
657 inhibitors to improve oral bioavailability and CNS penetration of anticancer drugs. *Trends in*
658 *pharmacological sciences* **2006**, *27*, (1), 17-24.
- 659 26. Allen, J. D.; van Loevezijn, A.; Lakhai, J. M.; van der Valk, M.; van Tellingen, O.;
660 Reid, G.; Schellens, J. H. M.; Koomen, G. J.; Schinkel, A. H. Potent and Specific Inhibition
661 of the Breast Cancer Resistance Protein Multidrug Transporter in Vitro and in Mouse
662 Intestine by a Novel Analogue of Fumitremorgin C 1 This work was supported in part by
663 grant NKI 97-1433 from the Dutch Cancer Society (to AHS). Synthesis investigations by A.
664 v. L. and GJ. K. were supported by the Netherlands Research Council for Chemical Sciences
665 (NWO/CW) and the Netherlands Technology Foundation (STW). 1. *Molecular cancer*
666 *therapeutics* **2002**, *1*, (6), 417-425.
- 667 27. Ashida, H.; Fukuda, I.; Yamashita, T.; Kanazawa, K. Flavones and flavonols at
668 dietary levels inhibit a transformation of aryl hydrocarbon receptor induced by dioxin. *FEBS*
669 *letters* **2000**, *476*, (3), 213-7.
- 670 28. Pick, A.; Müller, H.; Mayer, R.; Haenisch, B.; Pajeva, I. K.; Weigt, M.; Bönisch, H.;
671 Müller, C. E.; Wiese, M. Structure-activity relationships of flavonoids as inhibitors of breast
672 cancer resistance protein (BCRP). *Bioorganic & Medicinal Chemistry* **2011**, *19*, (6), 2090-
673 2102.
- 674 29. Fleisher, B.; Unum, J.; Shao, J.; An, G. Ingredients in Fruit Juices Interact with
675 Dasatinib Through Inhibition of BCRP: A New Mechanism of Beverage-Drug Interaction.
676 *Journal of Pharmaceutical Sciences* **2015**, *104*, (1), 266-275.
- 677 30. Zhang, S.; Yang, X.; Morris, M. E. Flavonoids are inhibitors of breast cancer
678 resistance protein (ABCG2)-mediated transport. *Molecular pharmacology* **2004**, *65*, (5),
679 1208-1216.

- 680 31. van Zanden, J. J.; van der Woude, H.; Vaessen, J.; Usta, M.; Wortelboer, H. M.;
681 Cnubben, N. H. P.; Rietjens, I. M. C. M. The effect of quercetin phase II metabolism on its
682 MRP1 and MRP2 inhibiting potential. *Biochemical pharmacology* **2007**, *74*, (2), 345-351.
- 683 32. Zhang, S.; Wang, X.; Sagawa, K.; Morris, M. E. Flavonoids chrysin and
684 benzoflavone, potent breast cancer resistance protein inhibitors, have no significant effect on
685 topotecan pharmacokinetics in rats or *mdr1a/1b* (-/-) mice. *Drug metabolism and disposition: the biological fate of chemicals* **2005**, *33*, (3), 341-8.
- 687 33. Robey, R. W.; Steadman, K.; Polgar, O.; Morisaki, K.; Blayney, M.; Mistry, P.;
688 Bates, S. E. Pheophorbide a is a specific probe for ABCG2 function and inhibition. *Cancer*
689 *research* **2004**, *64*, (4), 1242-1246.
- 690 34. Ferrandiz, M. L.; Alcaraz, M. J. Anti-inflammatory activity and inhibition of
691 arachidonic acid metabolism by flavonoids. *Agents and actions* **1991**, *32*, (3-4), 283-8.
- 692 35. Breedveld, P.; Beijnen, J. H.; Schellens, J. H. Use of P-glycoprotein and BCRP
693 inhibitors to improve oral bioavailability and CNS penetration of anticancer drugs. *Trends in*
694 *pharmacological sciences* **2006**, *27*, (1), 17-24.
- 695 36. Allen, J. D.; van Loevezijn, A.; Lakhai, J. M.; van der Valk, M.; van Tellingen, O.;
696 Reid, G.; Schellens, J. H.; Koomen, G. J.; Schinkel, A. H. Potent and specific inhibition of
697 the breast cancer resistance protein multidrug transporter in vitro and in mouse intestine by a
698 novel analogue of fumitremorgin C. *Molecular cancer therapeutics* **2002**, *1*, (6), 417-25.
- 699 37. Gupta, V.; Aseh, A.; Rios, C. N.; Aggarwal, B. B.; Mathur, A. B. Fabrication and
700 characterization of silk fibroin-derived curcumin nanoparticles for cancer therapy.
701 *International journal of nanomedicine* **2009**, *4*, 115-22.
- 702 38. Gupta, N. K.; Dixit, V. K. Development and evaluation of vesicular system for
703 curcumin delivery. *Arch Dermatol Res* **2011**, *303*, (2), 89-101.
- 704 39. Gupta, N. K.; Dixit, V. K. Bioavailability enhancement of curcumin by complexation
705 with phosphatidyl choline. *J Pharm Sci* **2011**, *100*, (5), 1987-95.
- 706 40. Krausz, A. E.; Adler, B. L.; Cabral, V.; Navati, M.; Doerner, J.; Charafeddine, R. A.;
707 Chandra, D.; Liang, H.; Gunther, L.; Clendaniel, A.; Harper, S.; Friedman, J. M.; Nosanchuk,
708 J. D.; Friedman, A. J. Curcumin-encapsulated nanoparticles as innovative antimicrobial and
709 wound healing agent. *Nanomedicine: Nanotechnology, Biology and Medicine* **2015**, *11*, (1),
710 195-206.
- 711 41. Mohammadian, F.; Pilehvar-Soltanahmadi, Y.; Mofarrah, M.; Dastani-Habashi, M.;
712 Zarghami, N. Down regulation of miR-18a, miR-21 and miR-221 genes in gastric cancer cell
713 line by chrysin-loaded PLGA-PEG nanoparticles. *Artificial cells, nanomedicine, and*
714 *biotechnology* **2016**, 1-7.
- 715 42. Zhu, Z. Y.; Luo, Y.; Liu, Y.; Wang, X. T.; Liu, F.; Guo, M. Z.; Wang, Z.; Liu, A. J.;
716 Zhang, Y. M. Inclusion of chrysin in beta-cyclodextrin and its biological activities. *J Drug*
717 *Deliv Sci Tec* **2016**, *31*, 176-186.
- 718 43. Chakraborty, S.; Basu, S.; Lahiri, A.; Basak, S. Inclusion of chrysin in beta-
719 cyclodextrin nanocavity and its effect on antioxidant potential of chrysin: A spectroscopic
720 and molecular modeling approach. *J Mol Struct* **2010**, *977*, (1-3), 180-188.
- 721 44. Bottini, M.; D'Annibale, F.; Magrini, A.; Cerignoli, F.; Arimura, Y.; Dawson, M. I.;
722 Bergamaschi, E.; Rosato, N.; Bergamaschi, A.; Mustelin, T. Quantum dot-doped silica
723 nanoparticles as probes for targeting of T-lymphocytes. *International journal of*
724 *nanomedicine* **2007**, *2*, (2), 227-33.
- 725 45. Gerion, D.; Herberg, J.; Bok, R.; Gjersing, E.; Ramon, E.; Maxwell, R.; Kurhanewicz,
726 J.; Budinger, T. F.; Gray, J. W.; Shuman, M. A.; Chen, F. F. Paramagnetic Silica-Coated
727 Nanocrystals as an Advanced MRI Contrast Agent. *The Journal of Physical Chemistry C*
728 **2007**, *111*, (34), 12542-12551.

- 729 46. Nehoff, H.; Parayath, N. N.; Domanovitch, L.; Taurin, S.; Greish, K. Nanomedicine
730 for drug targeting: strategies beyond the enhanced permeability and retention effect.
731 *International journal of nanomedicine* **2014**, *9*, 2539-2555.
- 732 47. Liao, Y.-T.; Liu, C.-H.; Yu, J.; Wu, K. C. Liver cancer cells: targeting and
733 prolonged-release drug carriers consisting of mesoporous silica nanoparticles and alginate
734 microspheres. *International journal of nanomedicine* **2014**, *9*, 2767.
- 735 48. Marzaioli, V.; Aguilar-Pimentel, J. A.; Weichenmeier, I.; Luxenhofer, G.; Wiemann,
736 M.; Landsiedel, R.; Wohlleben, W.; Eiden, S.; Mempel, M.; Behrendt, H. Surface
737 modifications of silica nanoparticles are crucial for their inert versus proinflammatory and
738 immunomodulatory properties. *Int J Nanomed* **2014**, *9*, 2815-2832.
- 739 49. Kresge, C. T.; Leonowicz, M. E.; Roth, W. J.; Vartuli, J. C.; Beck, J. S. Ordered
740 Mesoporous Molecular-Sieves Synthesized by a Liquid-Crystal Template Mechanism.
741 *Nature* **1992**, *359*, (6397), 710-712.
- 742 50. Slowing, I. I.; Vivero-Escoto, J. L.; Wu, C.-W.; Lin, V. S. Y. Mesoporous silica
743 nanoparticles as controlled release drug delivery and gene transfection carriers. *Advanced*
744 *Drug Delivery Reviews* **2008**, *60*, (11), 1278-1288.
- 745 51. Kim, S.; Philippot, S.; Fontanay, S.; Duval, R. E.; Lamouroux, E.; Canilho, N.; Pasc,
746 A. pH- and glutathione-responsive release of curcumin from mesoporous silica nanoparticles
747 coated using tannic acid-Fe(III) complex. *RSC Advances* **2015**, *5*, (110), 90550-90558.
- 748 52. Illum, L. Transport of drugs from the nasal cavity to the central nervous system.
749 *European journal of pharmaceutical sciences : official journal of the European Federation*
750 *for Pharmaceutical Sciences* **2000**, *11*, (1), 1-18.
- 751 53. Pires, A.; Fortuna, A.; Alves, G.; Falcão, A. Intranasal drug delivery: how, why and
752 what for? *Journal of Pharmacy & Pharmaceutical Sciences* **2009**, *12*, (3), 288-311.
- 753 54. Gizurarson, S. Anatomical and histological factors affecting intranasal drug and
754 vaccine delivery. *Current drug delivery* **2012**, *9*, (6), 566-82.
- 755 55. Purves, D., *Neuroscience*. 4th ed. / edited by Dale Purves ... [et al.]. ed.; W. H.
756 Freeman ; Basingstoke : Palgrave [distributor]: New York, 2007.
- 757 56. Frey, W. H. Method for administering neurologic agents to the brain. US 5624898 A,
758 1997.
- 759 57. Frey, W. H. Neurologic agents for nasal administration to the brain. WO1991007947
760 A1, 1997.
- 761 58. Frey, W. H. Method for administering insulin to the brain. US 6313093 B1, 2001.
- 762 59. Choudhury, D.; Ganguli, A.; Dastidar, D. G.; Acharya, B. R.; Das, A.; Chakrabarti, G.
763 Apigenin shows synergistic anticancer activity with curcumin by binding at different sites of
764 tubulin. *Biochimie* **2013**, *95*, (6), 1297-309.
- 765 60. Monroy, A.; Lithgow, G. J.; Alavez, S. Curcumin and neurodegenerative diseases.
766 *Biofactors* **2013**, *39*, (1), 122-132.
- 767 61. Mythri, R. B.; Harish, G.; Dubey, S. K.; Misra, K.; Bharath, M. M. Glutamoyl diester
768 of the dietary polyphenol curcumin offers improved protection against peroxynitrite-mediated
769 nitrosative stress and damage of brain mitochondria in vitro: implications for Parkinson's
770 disease. *Mol Cell Biochem* **2011**, *347*, (1-2), 135-43.
- 771 62. Zbarsky, V.; Datla, K. P.; Parkar, S.; Rai, D. K.; Aruoma, O. I.; Dexter, D. T.
772 Neuroprotective properties of the natural phenolic antioxidants curcumin and naringenin but
773 not quercetin and fisetin in a 6-OHDA model of Parkinson's disease. *Free Radical Res* **2005**,
774 *39*, (10), 1119-1125.
- 775 63. Yao, Y.; Chen, L.; Xiao, J.; Wang, C.; Jiang, W.; Zhang, R.; Hao, J. Chrysin protects
776 against focal cerebral ischemia/reperfusion injury in mice through attenuation of oxidative
777 stress and inflammation. *International journal of molecular sciences* **2014**, *15*, (11), 20913-
778 26.

- 779 64. Xiao, J.; Zhai, H.; Yao, Y.; Wang, C.; Jiang, W.; Zhang, C.; Simard, A. R.; Zhang, R.;
780 Hao, J. Chrysin attenuates experimental autoimmune neuritis by suppressing immuno-
781 inflammatory responses. *Neuroscience* **2014**, *262*, 156-64.
- 782 65. Souza, L. C.; Antunes, M. S.; Filho, C. B.; Del Fabbro, L.; de Gomes, M. G.; Goes,
783 A. T.; Donato, F.; Prigol, M.; Boeira, S. P.; Jesse, C. R. Flavonoid Chrysin prevents age-
784 related cognitive decline via attenuation of oxidative stress and modulation of BDNF levels
785 in aged mouse brain. *Pharmacology, biochemistry, and behavior* **2015**, *134*, 22-30.
- 786 66. Santos, B. L.; Oliveira, M. N.; Coelho, P. L.; Pitanga, B. P.; da Silva, A. B.; Adelita,
787 T.; Silva, V. D.; Costa Mde, F.; El-Bacha, R. S.; Tardy, M.; Chneiweiss, H.; Junier, M. P.;
788 Moura-Neto, V.; Costa, S. L. Flavonoids suppress human glioblastoma cell growth by
789 inhibiting cell metabolism, migration, and by regulating extracellular matrix proteins and
790 metalloproteinases expression. *Chemico-biological interactions* **2015**, *242*, 123-38.
- 791 67. Nabavi, S. F.; Braidly, N.; Habtemariam, S.; Orhan, I. E.; Daglia, M.; Manayi, A.;
792 Gortzi, O.; Nabavi, S. M. Neuroprotective effects of chrysin: From chemistry to medicine.
793 *Neurochemistry international* **2015**, *90*, 224-31.
- 794 68. Jia, W. Z.; Zhao, J. C.; Sun, X. L.; Yao, Z. G.; Wu, H. L.; Xi, Z. Q. Additive
795 anticancer effects of chrysin and low dose cisplatin in human malignant glioma cell (U87)
796 proliferation and evaluation of the mechanistic pathway. *Journal of B.U.ON. : official journal*
797 *of the Balkan Union of Oncology* **2015**, *20*, (5), 1327-36.
- 798 69. Fan, J.; Fang, G.; Wang, X.; Zeng, F.; Xiang, Y.; Wu, S. Targeted anticancer prodrug
799 with mesoporous silica nanoparticles as vehicles. *Nanotechnology* **2011**, *22*, (45), 455102.
- 800 70. Brunauer, S.; Emmett, P. H.; Teller, E. Adsorption of Gases in Multimolecular
801 Layers. *Journal of the American Chemical Society* **1938**, *60*, (2), 309-319.
- 802 71. Uebing-Czipura, A. U.; Dawson, H. D.; Scherba, G. Immortalization and
803 characterization of lineage-restricted neuronal progenitor cells derived from the porcine
804 olfactory bulb. *Journal of neuroscience methods* **2008**, *170*, (2), 262-76.
- 805 72. Li, J.; Jiang, Y.; Wen, J.; Fan, G.; Wu, Y.; Zhang, C. A rapid and simple HPLC
806 method for the determination of curcumin in rat plasma: assay development, validation and
807 application to a pharmacokinetic study of curcumin liposome. *Biomedical Chromatography*
808 **2009**, *23*, (11), 1201-1207.
- 809 73. Zaveri, M.; Khandhar, A.; Jain, S. Quantification of baicalein, chrysin, biochanin-A
810 and ellagic acid in root bark of *Oroxylum indicum* by RP-HPLC with UV detection. *Eurasian*
811 *Journal of Analytical Chemistry* **2008**, *3*, (2), 245-257.
- 812 74. Yallapu, M. M.; Gupta, B. K.; Jaggi, M.; Chauhan, S. C. Fabrication of curcumin
813 encapsulated PLGA nanoparticles for improved therapeutic effects in metastatic cancer cells.
814 *J Colloid Interf Sci* **2010**, *351*, (1), 19-29.
- 815 75. Hao, N.; Jayawardana, K. W.; Chen, X.; Yan, M. One-step synthesis of amine-
816 functionalized hollow mesoporous silica nanoparticles as efficient antibacterial and
817 anticancer materials. *ACS applied materials & interfaces* **2015**, *7*, (2), 1040-1045.
- 818 76. He, Q.; Zhang, J.; Shi, J.; Zhu, Z.; Zhang, L.; Bu, W.; Guo, L.; Chen, Y. The effect of
819 PEGylation of mesoporous silica nanoparticles on nonspecific binding of serum proteins and
820 cellular responses. *Biomaterials* **2010**, *31*, (6), 1085-1092.
- 821 77. Wu, X.; Han, Z.; Schur, R. M.; Lu, Z.-R. Targeted Mesoporous Silica Nanoparticles
822 Delivering Arsenic Trioxide with Environment Sensitive Drug Release for Effective
823 Treatment of Triple Negative Breast Cancer. *ACS Biomaterials Science & Engineering* **2016**,
824 *2*, (4), 501-507.
- 825 78. Feng, R.; Song, Z.; Zhai, G. Preparation and in vivo pharmacokinetics of curcumin-
826 loaded PCL-PEG-PCL triblock copolymeric nanoparticles. *International journal of*
827 *nanomedicine* **2012**, *7*, 4089-98.

828 79. Jambhrunkar, S.; Karmakar, S.; Popat, A.; Yu, M. H.; Yu, C. Z. Mesoporous silica
829 nanoparticles enhance the cytotoxicity of curcumin. *Rsc Advances* **2014**, *4*, (2), 709-712.

830 80. Khan, M. A.; Akhtar, N.; Sharma, V.; Pathak, K. Product development studies on
831 sonocrystallized curcumin for the treatment of gastric cancer. *Pharmaceutics* **2015**, *7*, (2), 43-
832 63.

833 81. Zeng, Y. B.; Yang, N.; Liu, W. S.; Tang, N. Synthesis, characterization and DNA-
834 binding properties of La(III) complex of chrysin. *J Inorg Biochem* **2003**, *97*, (3), 258-264.

835 82. Lee, C.-H.; Lo, L.-W.; Mou, C.-Y.; Yang, C.-S. Synthesis and Characterization of
836 Positive-Charge Functionalized Mesoporous Silica Nanoparticles for Oral Drug Delivery of
837 an Anti-Inflammatory Drug. *Advanced Functional Materials* **2008**, *18*, (20), 3283-3292.

838 83. Chung, T. H.; Wu, S. H.; Yao, M.; Lu, C. W.; Lin, Y. S.; Hung, Y.; Mou, C. Y.;
839 Chen, Y. C.; Huang, D. M. The effect of surface charge on the uptake and biological
840 function of mesoporous silica nanoparticles in 3T3-L1 cells and human mesenchymal stem
841 cells. *Biomaterials* **2007**, *28*, (19), 2959-66.

842 84. DeMuth, P.; Hurley, M.; Wu, C.; Galanie, S.; Zachariah, M. R.; DeShong, P.
843 Mesoscale porous silica as drug delivery vehicles: Synthesis, characterization, and pH-
844 sensitive release profiles. *Micropor Mesopor Mat* **2011**, *141*, (1-3), 128-134.

845 85. Farghali, A.; Swiderska-Sroda, A.; Lojkowski, W.; Razin, A.-F. M.; Khedr, M.;
846 AbouAitah, K. E. pH-controlled Release System for Curcumin based on Functionalized
847 Dendritic Mesoporous Silica Nanoparticles. *Journal of Nanomedicine & Nanotechnology*
848 **2016**, *2016*.

849 86. Wang, Z.; Fan, H.; Li, Y.; Wang, Y. Anti-hepatocarcinoma effects of chrysin loaded
850 solid lipid nanoparticle against H22 tumor bearing mice. **2015**.

851 87. Sathishkumar, G.; Bharti, R.; Jha, P. K.; Selvakumar, M.; Dey, G.; Jha, R.; Jeyaraj,
852 M.; Mandal, M.; Sivaramakrishnan, S. Dietary flavone chrysin (5,7-dihydroxyflavone ChR)
853 functionalized highly-stable metal nanoformulations for improved anticancer applications.
854 *RSC Advances* **2015**, *5*, (109), 89869-89878.

855 88. Cooper, G., *The Cell: A Molecular Approach. 2nd edition.* 2 ed.; Sinauer Associates:
856 Sunderland (MA), 2000.

857 89. Taebnia, N.; Morshedi, D.; Doostkam, M.; Yaghmaei, S.; Aliakbari, F.; Singh, G.;
858 Arpanaei, A. The effect of mesoporous silica nanoparticle surface chemistry and
859 concentration on the alpha-synuclein fibrillation. *Rsc Advances* **2015**, *5*, (75), 60966-60974.

860 90. Huang, X. Y.; Young, N. P.; Townley, H. E. Characterization and Comparison of
861 Mesoporous Silica Particles for Optimized Drug Delivery. *Nanomater Nanotechno* **2014**, *4*.

862 91. Boussif, O.; Lezoualch, F.; Zanta, M. A.; Mergny, M. D.; Scherman, D.; Demeneix,
863 B.; Behr, J. P. A Versatile Vector for Gene and Oligonucleotide Transfer into Cells in
864 Culture and in-Vivo - Polyethylenimine. *Proceedings of the National Academy of Sciences of*
865 *the United States of America* **1995**, *92*, (16), 7297-7301.

866 92. Wanyika, H.; Gatebe, E.; Kioni, P.; Tang, Z. Y.; Gao, Y. Synthesis and
867 characterization of ordered mesoporous silica nanoparticles with tunable physical properties
868 by varying molar composition of reagents. *Afr J Pharm Pharmacol* **2011**, *5*, (21), 2402-2410.

869 93. Salonen, J.; Laitinen, L.; Kaukonen, A. M.; Tuura, J.; Bjorkqvist, M.; Heikkila, T.;
870 Vaha-Heikkila, K.; Hirvonen, J.; Lehto, V. P. Mesoporous silicon microparticles for oral
871 drug delivery: Loading and release of five model drugs. *Journal of Controlled Release* **2005**,
872 *108*, (2-3), 362-374.

873 94. Napierska, D.; Thomassen, L. C.; Rabolli, V.; Lison, D.; Gonzalez, L.;
874 Kirsch-Volders, M.; Martens, J. A.; Hoet, P. H. Size-Dependent Cytotoxicity of
875 Monodisperse Silica Nanoparticles in Human Endothelial Cells. *Small* **2009**, *5*, (7), 846-853.

876 95. Ye, Y.; Liu, J.; Chen, M.; Sun, L.; Lan, M. In vitro toxicity of silica nanoparticles in
877 myocardial cells. *Environmental toxicology and pharmacology* **2010**, *29*, (2), 131-137.

- 878 96. Lin, W.; Huang, Y.-w.; Zhou, X.-D.; Ma, Y. In vitro toxicity of silica nanoparticles
879 in human lung cancer cells. *Toxicology and applied pharmacology* **2006**, *217*, (3), 252-259.
- 880 97. Oberdörster, G.; Oberdörster, E.; Oberdörster, J. Nanotoxicology: an emerging
881 discipline evolving from studies of ultrafine particles. *Environmental health perspectives*
882 **2005**, 823-839.
- 883 98. Kipen, H. M.; Laskin, D. L. Smaller is not always better: nanotechnology yields
884 nanotoxicology. *American Journal of Physiology-Lung Cellular and Molecular Physiology*
885 **2005**, *289*, (5), L696-L697.
- 886 99. Nel, A.; Xia, T.; Mädler, L.; Li, N. Toxic potential of materials at the nanolevel.
887 *Science (New York, N.Y.)* **2006**, *311*, (5761), 622-627.
- 888 100. Lu, X.; Qian, J.; Zhou, H.; Gan, Q.; Tang, W.; Lu, J.; Yuan, Y.; Liu, C. In vitro
889 cytotoxicity and induction of apoptosis by silica nanoparticles in human HepG2 hepatoma
890 cells. *International journal of nanomedicine* **2011**, *6*, 1889-1901.
- 891 101. Barrett, E. G.; Johnston, C.; Oberdörster, G.; Finkelstein, J. N. Silica binds serum
892 proteins resulting in a shift of the dose-response for silica-induced chemokine expression in
893 an alveolar type II cell line. *Toxicology and applied pharmacology* **1999**, *161*, (2), 111-122.
- 894 102. Cedervall, T.; Lynch, I.; Foy, M.; Berggård, T.; Donnelly, S. C.; Cagney, G.; Linse,
895 S.; Dawson, K. A. Detailed identification of plasma proteins adsorbed on copolymer
896 nanoparticles. *Angewandte Chemie* **2007**, *119*, (30), 5856-5858.
- 897 103. Mukerjee, A.; Vishwanatha, J. K. Formulation, characterization and evaluation of
898 curcumin-loaded PLGA nanospheres for cancer therapy. *Anticancer research* **2009**, *29*, (10),
899 3867-75.
- 900 104. Yu, K. O.; Grabinski, C. M.; Schrand, A. M.; Murdock, R. C.; Wang, W.; Gu, B. H.;
901 Schlager, J. J.; Hussain, S. M. Toxicity of amorphous silica nanoparticles in mouse
902 keratinocytes. *J Nanopart Res* **2009**, *11*, (1), 15-24.
- 903 105. Mayor, S.; Pagano, R. E. Pathways of clathrin-independent endocytosis. *Nat Rev Mol*
904 *Cell Bio* **2007**, *8*, (8), 603-612.
- 905 106. Slowing, I. I.; Vivero-Escoto, J. L.; Wu, C. W.; Lin, V. S. Y. Mesoporous silica
906 nanoparticles as controlled release drug delivery and gene transfection carriers. *Advanced*
907 *Drug Delivery Reviews* **2008**, *60*, (11), 1278-1288.
- 908 107. Katz, L. C.; Burkhalter, A.; Dreyer, W. J. Fluorescent latex microspheres as a
909 retrograde neuronal marker for in vivo and in vitro studies of visual cortex. *Nature* **1984**, *310*,
910 (5977), 498-500.
- 911 108. Persson, H. G.; Gatzinsky, K. P. Distribution of retrogradely transported fluorescent
912 latex microspheres in rat lumbosacral ventral root axons following peripheral crush injury: a
913 light and electron microscopic study. *Brain Research* **1993**, *630*, (1-2), 115-124.
- 914 109. Katz, L. C.; Iarovici, D. M. Green fluorescent latex microspheres: A new retrograde
915 tracer. *Neuroscience* **1990**, *34*, (2), 511-520.
- 916 110. Huang, X.; Teng, X.; Chen, D.; Tang, F.; He, J. The effect of the shape of mesoporous
917 silica nanoparticles on cellular uptake and cell function. *Biomaterials*, **2010**, *31*, (3), 438-448.
- 918 111. Ma, X.; Teh, C.; Zhang, Q.; Borah, P.; Choong, C.; Korzh, V.; Zhao, Y. Redox-
919 Responsive Mesoporous Silica Nanoparticles: A Physiologically Sensitive Codelivery
920 Vehicle for siRNA and Doxorubicin. *Antioxidants & Redox Signaling* **2013**, *21*, (5), 707-722.
- 921 112. Meng, H.; Xue, M.; Xia, T.; Zhao, Y.-L.; Tamanoi, F.; Stoddart, J. F.; Zink, J.I.; Nel,
922 A. E. Autonomous in Vitro Anticancer Drug Release from Mesoporous Silica Nanoparticles
923 by pH-Sensitive Nanovalves. *Journal of the American Chemical Society* **2010**, *132*, (36),
924 12690-12697.
- 925 113. Huang, D. M.; Hung, Y.; Ko, B. S.; Hsu, S. C.; Chen, W. H.; Chien, C. L.; Tsai, C. P.;
926 Kuo, C. T.; Kang, J. C.; Yang, C. S.; Mou, C. Y.; Chen, Y. C. Highly efficient cellular

927 labeling of mesoporous nanoparticles in human mesenchymal stem cells: implication for stem
928 cell tracking. *Faseb Journal* **2005**, *19*, (12), 2014-6.

929 114. Anitha, A.; Deepagan, V. G.; Divya Rani, V. V.; Menon, D.; Nair, S. V.; Jayakumar,
930 R. Preparation, characterization, in vitro drug release and biological studies of curcumin
931 loaded dextran sulphate–chitosan nanoparticles. *Carbohydrate Polymers* **2011**, *84*, (3), 1158-
932 1164.

933 115. Zou, P.; Helson, L.; Maitra, A.; Stern, S. T.; McNeil, S. E. Polymeric Curcumin
934 Nanoparticle Pharmacokinetics and Metabolism in Bile Duct Cannulated Rats. *Molecular*
935 *Pharmaceutics* **2013**, *10*, (5), 1977-1987.

936 116. Yin, H.; Zhang, H.; Liu, B. Superior anticancer efficacy of curcumin-loaded
937 nanoparticles against lung cancer. *Acta Biochimica et Biophysica Sinica* **2013**.

938 117. Wang, Y. J.; Pan, M. H.; Cheng, A. L.; Lin, L. I.; Ho, Y. S.; Hsieh, C. Y.; Lin, J. K.
939 Stability of curcumin in buffer solutions and characterization of its degradation products. *J*
940 *Pharm Biomed Anal* **1997**, *15*, (12), 1867-76.

941 118. Tonnesen, H. H.; Karlsen, J. Studies on curcumin and curcuminoids. VI. Kinetics of
942 curcumin degradation in aqueous solution. *Z Lebensm Unters Forsch* **1985**, *180*, (5), 402-4.

943 119. Kunnumakkara, A. B.; Anand, P.; Aggarwal, B. B. Curcumin inhibits proliferation,
944 invasion, angiogenesis and metastasis of different cancers through interaction with multiple
945 cell signaling proteins. *Cancer letters* **2008**, *269*, (2), 199-225.

946 120. Lee, W. H.; Loo, C. Y.; Bebawy, M.; Luk, F.; Mason, R. S.; Rohanizadeh, R.
947 Curcumin and its derivatives: their application in neuropharmacology and neuroscience in the
948 21st century. *Current neuropharmacology* **2013**, *11*, (4), 338-78.

949 121. Gao, Y.; Chen, Y.; Ji, X.; He, X.; Yin, Q.; Zhang, Z.; Shi, J.; Li, Y. Controlled
950 intracellular release of doxorubicin in multidrug-resistant cancer cells by tuning the shell-
951 pore sizes of mesoporous silica nanoparticles. *ACS Nano* **2011**, *5*, (12), 9788-9798.

952

953 **LIST OF FIGURES**

954 **Figure 1:** MSNP particle sizing. (A) DLS particle size and PDI; (B) SEM image wide angle
955 view; (C) SEM image 60000x magnification.

956
957 **Figure 2:** FT-IR spectra of MSNP prior to CTAB removal (red) and immediately after CTAB
958 removal (black). CTAB and MSNP bands are indicated.

959
960 **Figure 3:** Surface porosity assessment of MSNP. (A) Nitrogen adsorption/desorption
961 isotherms of MSNP; (B) BJH pore radius distribution of MSNP. The Barrett Joyner-Halenda
962 pore sizes (Å: Ang) were calculated based on assessment of the cumulative pore volume (y-
963 axis) (red line) with the region corresponding to a pore diameter of 1-4 nm indicated by the
964 shaded box; (C) BJH pore width distribution of MSNP. The pore width (nm) were calculated
965 based on assessment of the cumulative pore volume. STP: standard temperature and
966 pressure.

967
968 **Figure 4:** FT-IR spectra of (A) Curcumin; (B) Curcumin loaded MSNP (Curc-MSNP).
969 (C) Chrysin; (D) Chrysin loaded MSNP (Chry-MSNP).

970
971 **Figure 5:** DSC thermogram of (A) curcumin and (B) chrysin as native drug (red) and MSNP
972 loaded (green). TGA thermograms (C) curcumin and (D) chrysin as native drug (red) and
973 MSNP loaded (green).

974
975 **Figure 6:** MSNP particle size and PDI before and after loading with curcumin (A and B) and
976 chrysin (C and D). Statistical significance tested between unloaded and loaded MSNP. * $P \leq$
977 0.05, ** $P \leq 0.01$.

978
979 **Figure 7:** Cellular toxicity of (A) MSNPs, (B) Curcumin and (C) Chrysin on OBGF 400
980 cells. Cells were grown on a 96-well plate at a density of 10×10^3 cells per well and exposed
981 to various concentrations of MSNP (10 – 1000 $\mu\text{g}/\text{mL}$) or phytochemicals (0.001-100 μM) .
982 After 24 hour incubation 100 μL MTT in PBS (0.5mg/mL) added to each well & incubated
983 for 4 hours. The MTT-formazan produced was solubilised in DMSO and quantified
984 colorimetrically using a UV-spectrophotometer at 570 nm. The control cell (without drug)
985 corresponded to a cell viability of 100%. Data is reported as mean \pm SD with up to 8
986 replicates per compound in at least 3 independent experiment. ** $P \leq 0.01$.

987
988 **Figure 8:** Confocal microscopy of latex bead uptake in OBGF400: A concentration of 0.1 %
989 v/v of latex beads (100 nm and 500 nm) were dispersed into HEPES (25mM) buffered HBSS
990 prior to the addition into wells containing OBGF 400 cells grown on collagen coated
991 coverslips. Beads were incubated for 2 hours before the coverslip were washed, fixed and
992 mounted onto coverslips with mounting media. Confocal microscopy was used to visualize
993 the cellular localisation of beads with a 40x (100 nm) or x63 (500 nm) oil immersion
994 objective. All images were acquired using an argon laser at 494 nm to visualise the beads and
995 a helium laser to visualise DAPI at 461 nm.

996
997 **Figure 9:** z-stack confocal microscopy of FITC-MSNP: FITC-MSNP previously incubated
998 with OBGF 400 cells for 2 hours were further subjected to a z-stack analysis with the lens
999 positioned above the cell layer (10763 μm) and lowered through the cells to the bottom of the
1000 cell layer (10758.4 μm). Individual images were captured of FITC (green) and DAPI (blue)
1001 through the z-dimension.

1002 **Figure 10:** Cumulative percentage release of (A) curcumin and (B) chrysin from MSNP. The
1003 *in vitro* release was performed in 154 mM PBS pH 7.4 and pH 5.5 containing 0.1 % Tween
1004 80. 1 mg/mL of phytochemical loaded MSNP were dispersed into 2 mL of release medium,
1005 briefly sonicated and placed in a shaking incubator maintained at 37 °C and 100 rpm.
1006 Samples were withdrawn at set time intervals and the volume replaced with an equal volume
1007 of pre-warmed release medium. Release was assessed through HPLC-UV methods. N=3. # #
1008 # indicates statistical comparison between the final time point (24 hours) and the first time
1009 point for (1 hour) for pH 5.5 with a $P \leq 0.001$. *** indicates statistical comparison between
1010 the final time point (24 hours) between pH 5.5 and 7.4 with a $P \leq 0.001$

1011

1012

1013

1014

1015

Figure 1

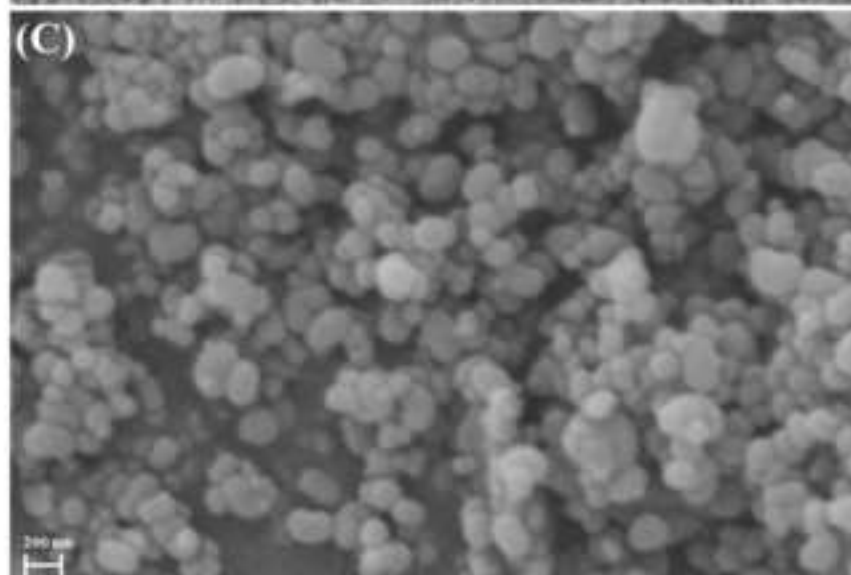
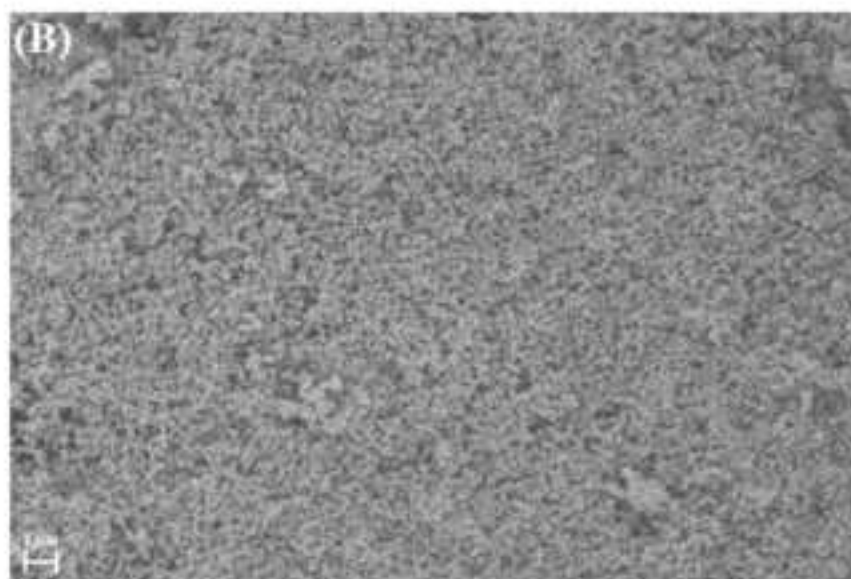
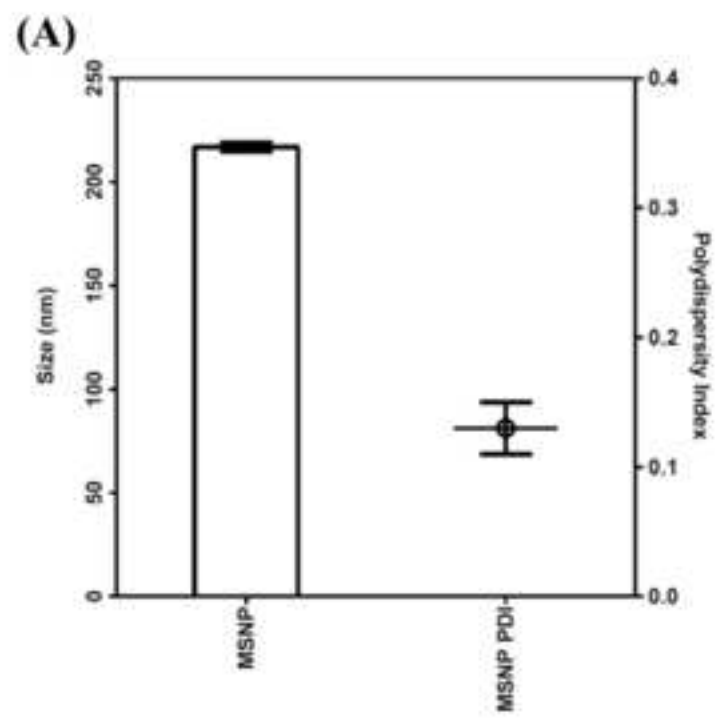


Figure 2

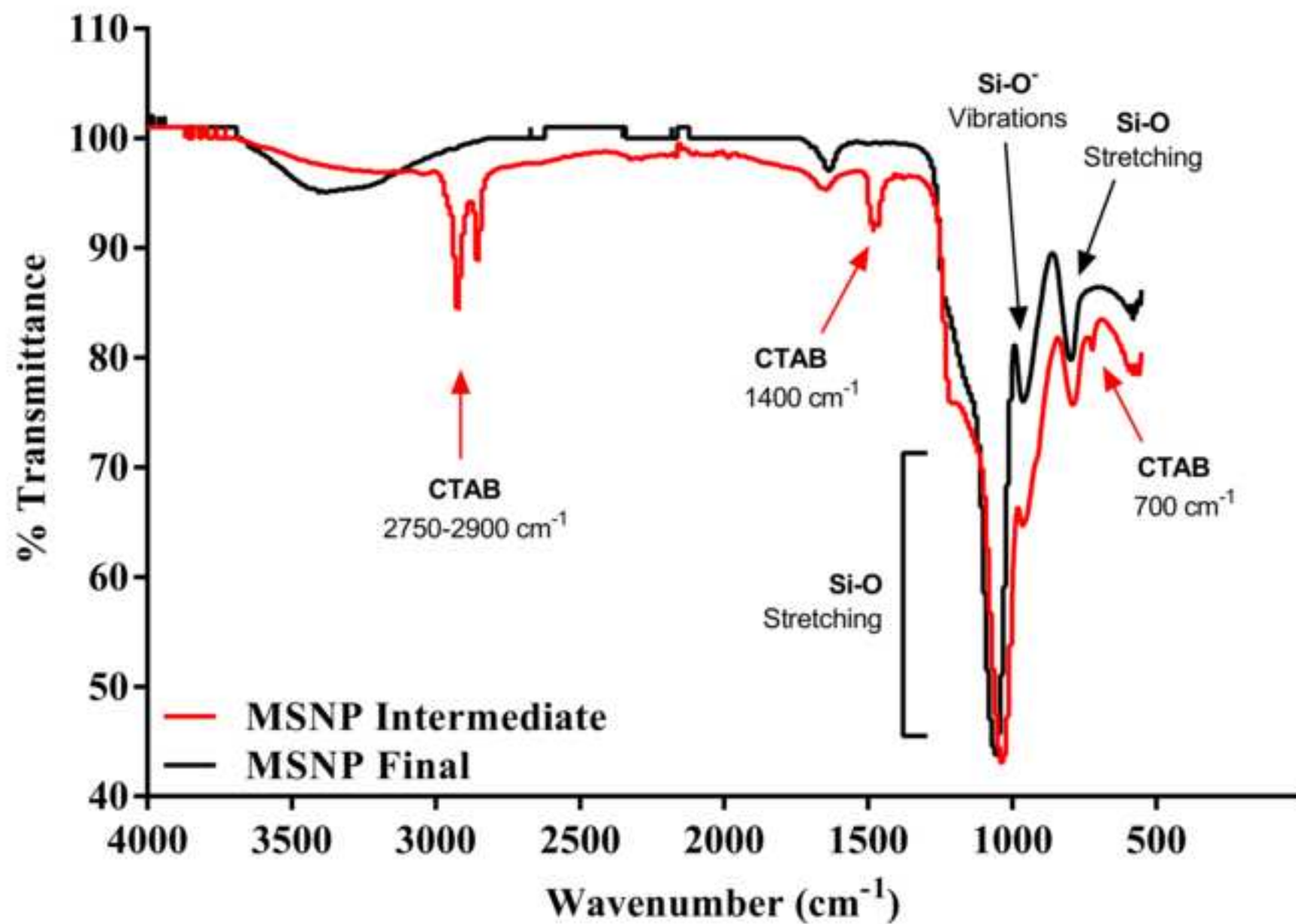


Figure 3

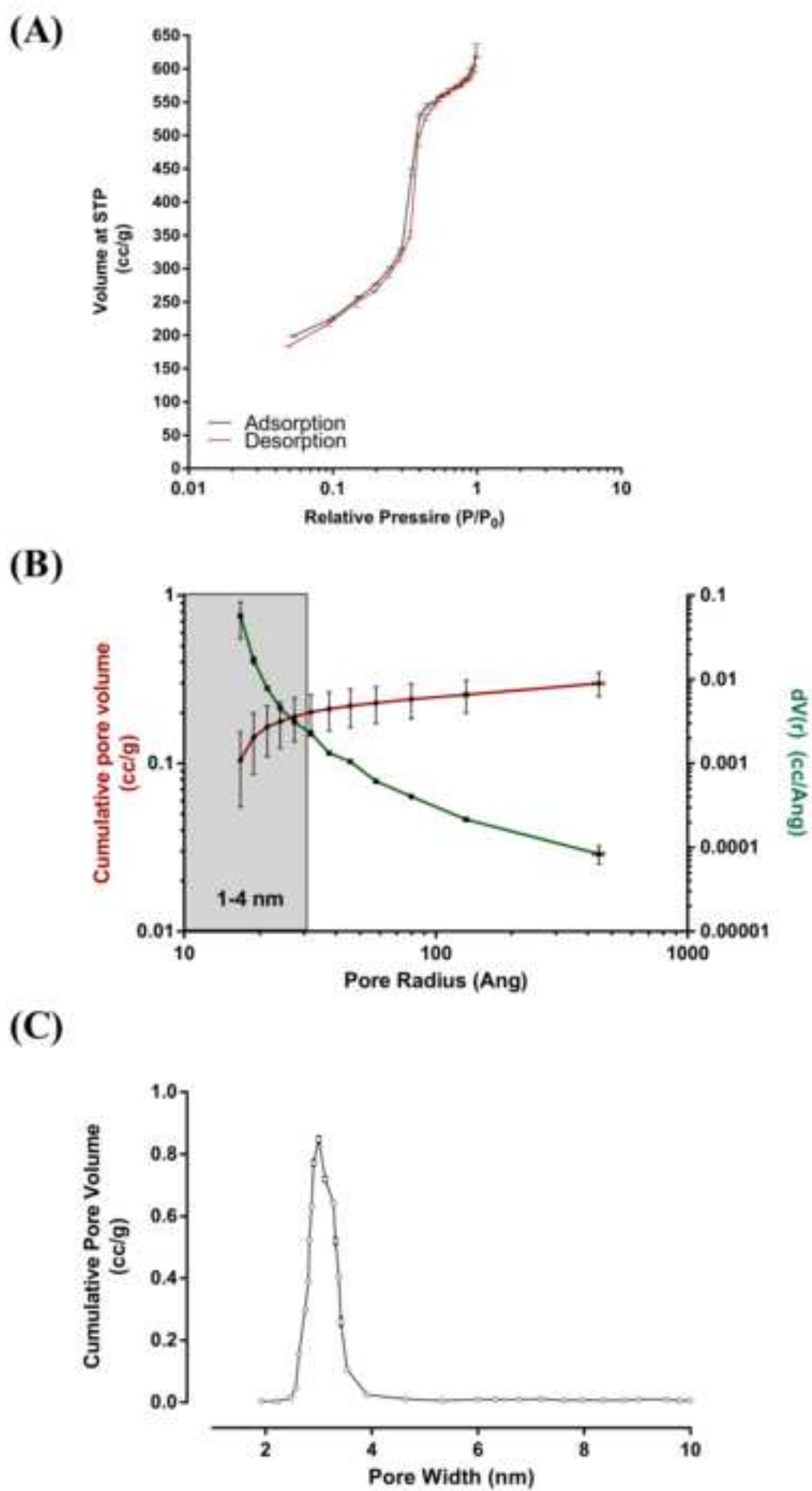
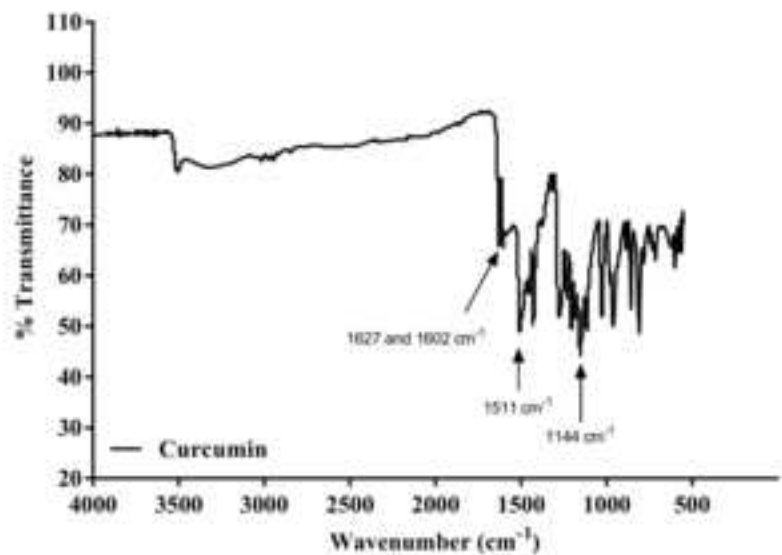
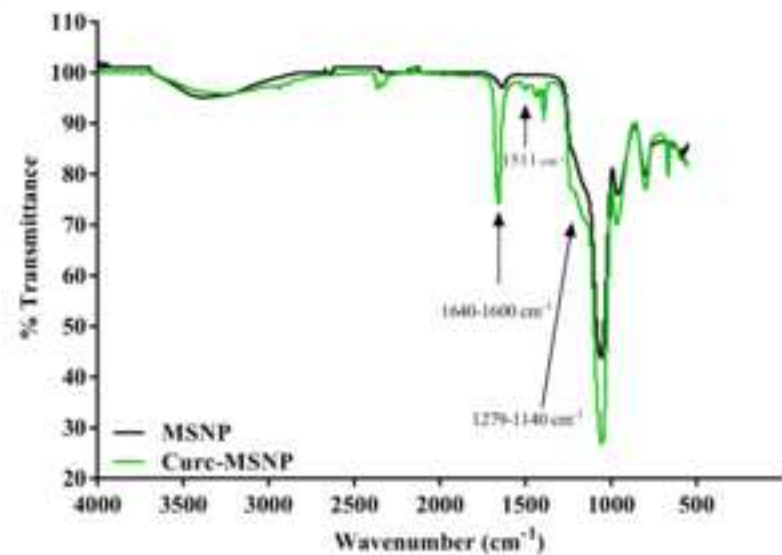


Figure 4

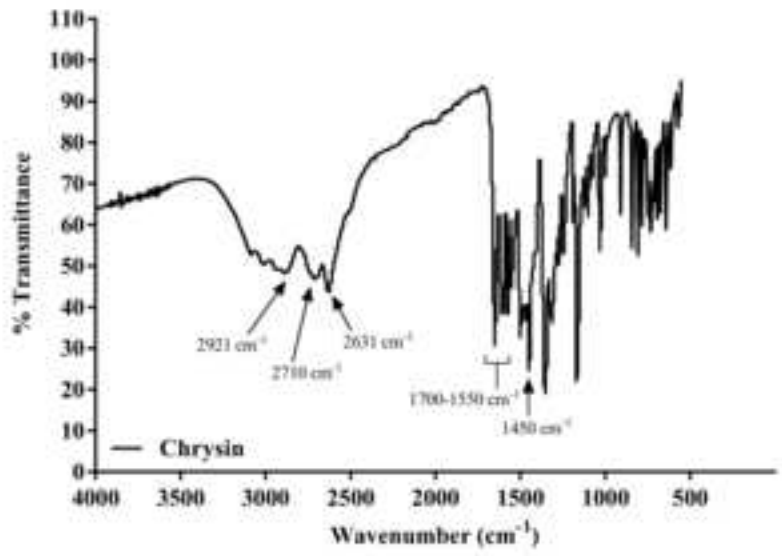
(A)



(B)



(C)



(D)

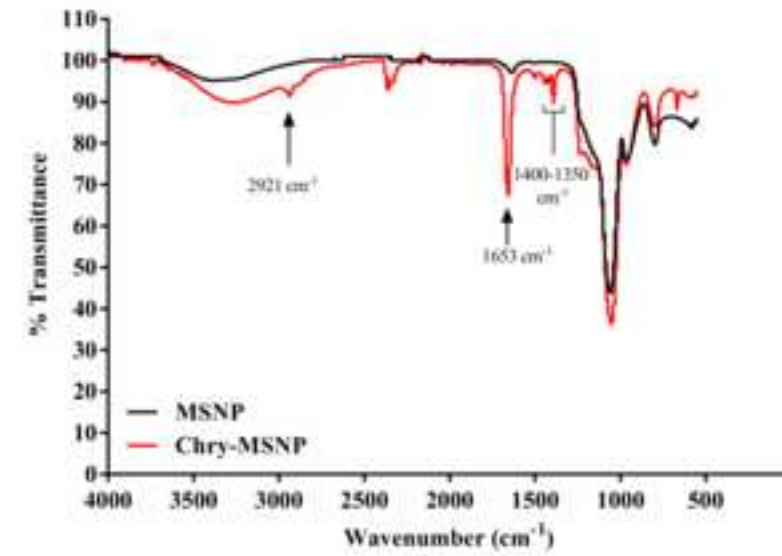


Figure 5

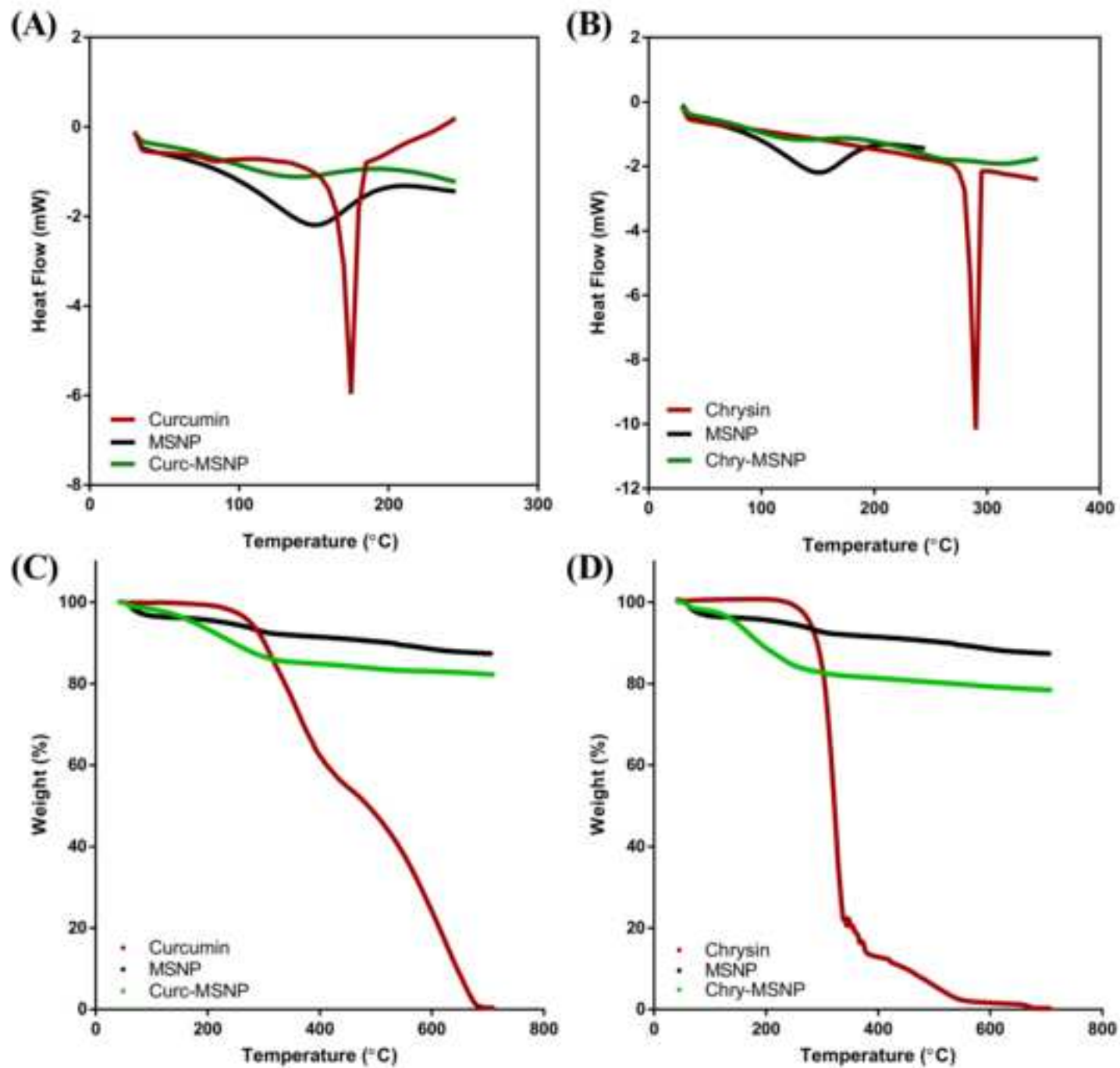


Figure 6

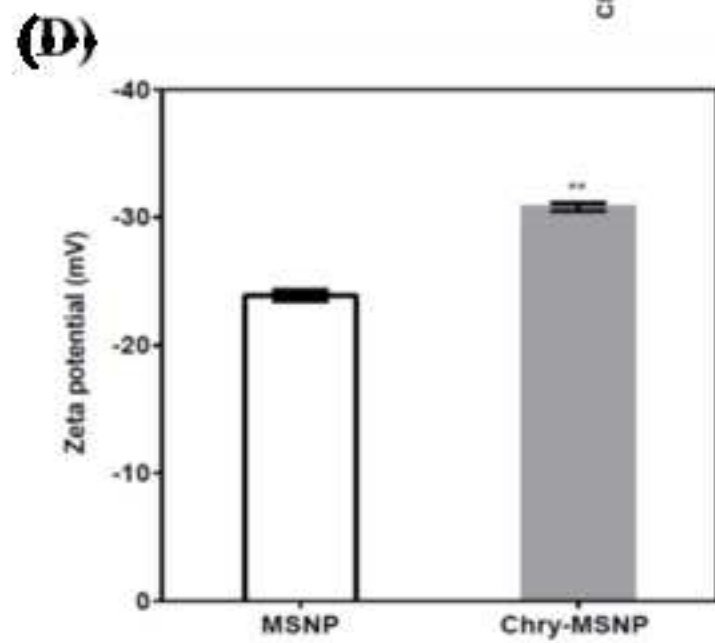
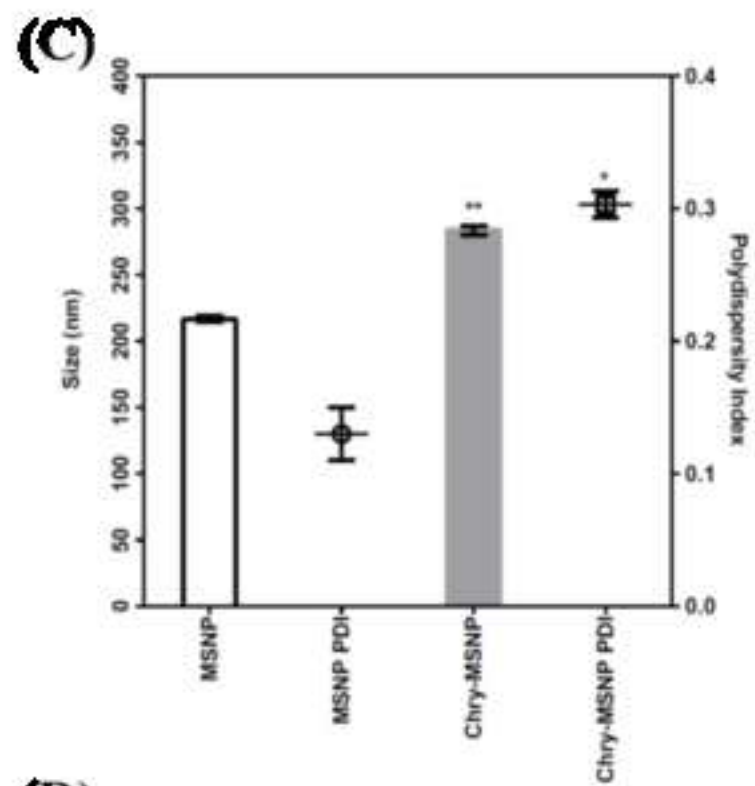
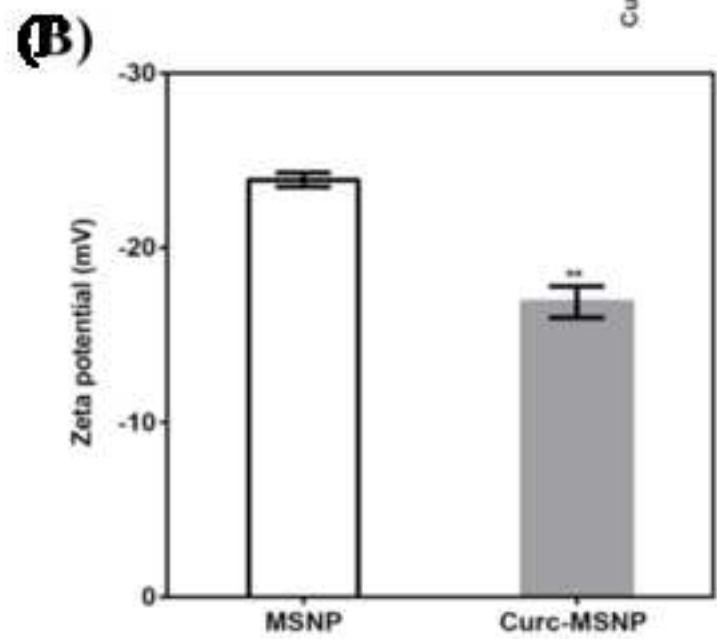
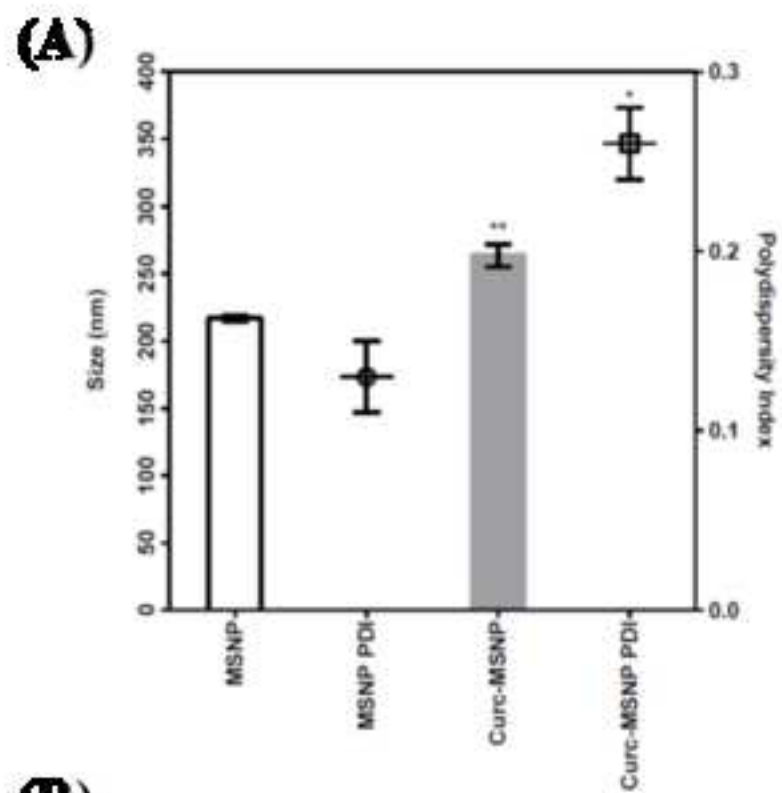


Figure 7

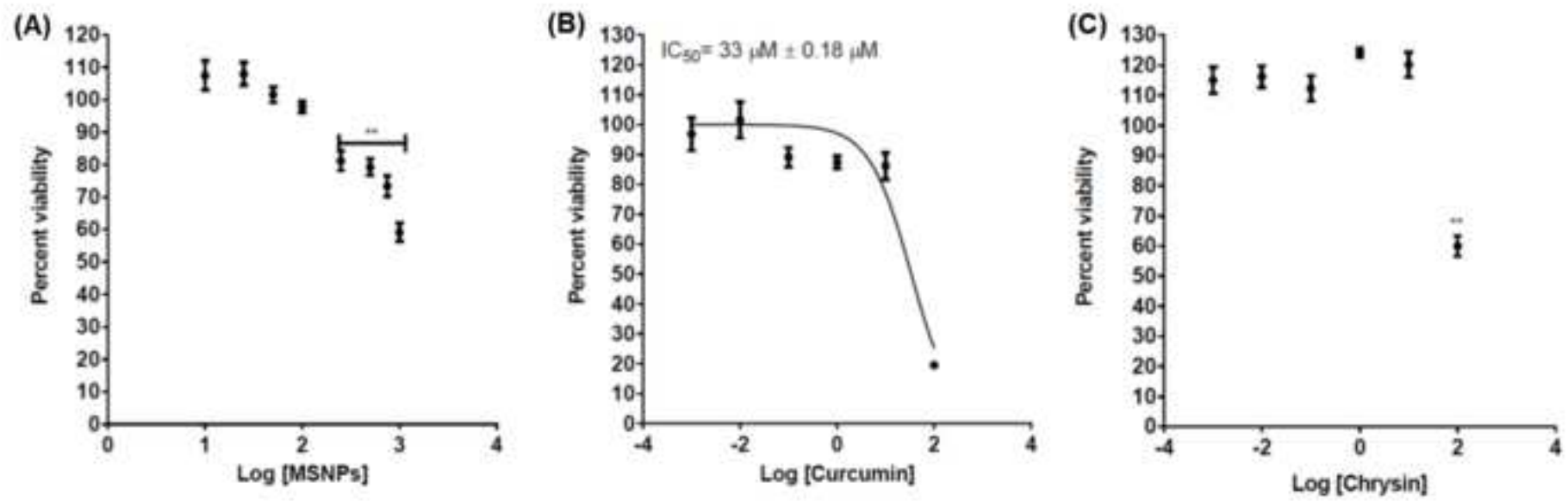


Figure 8

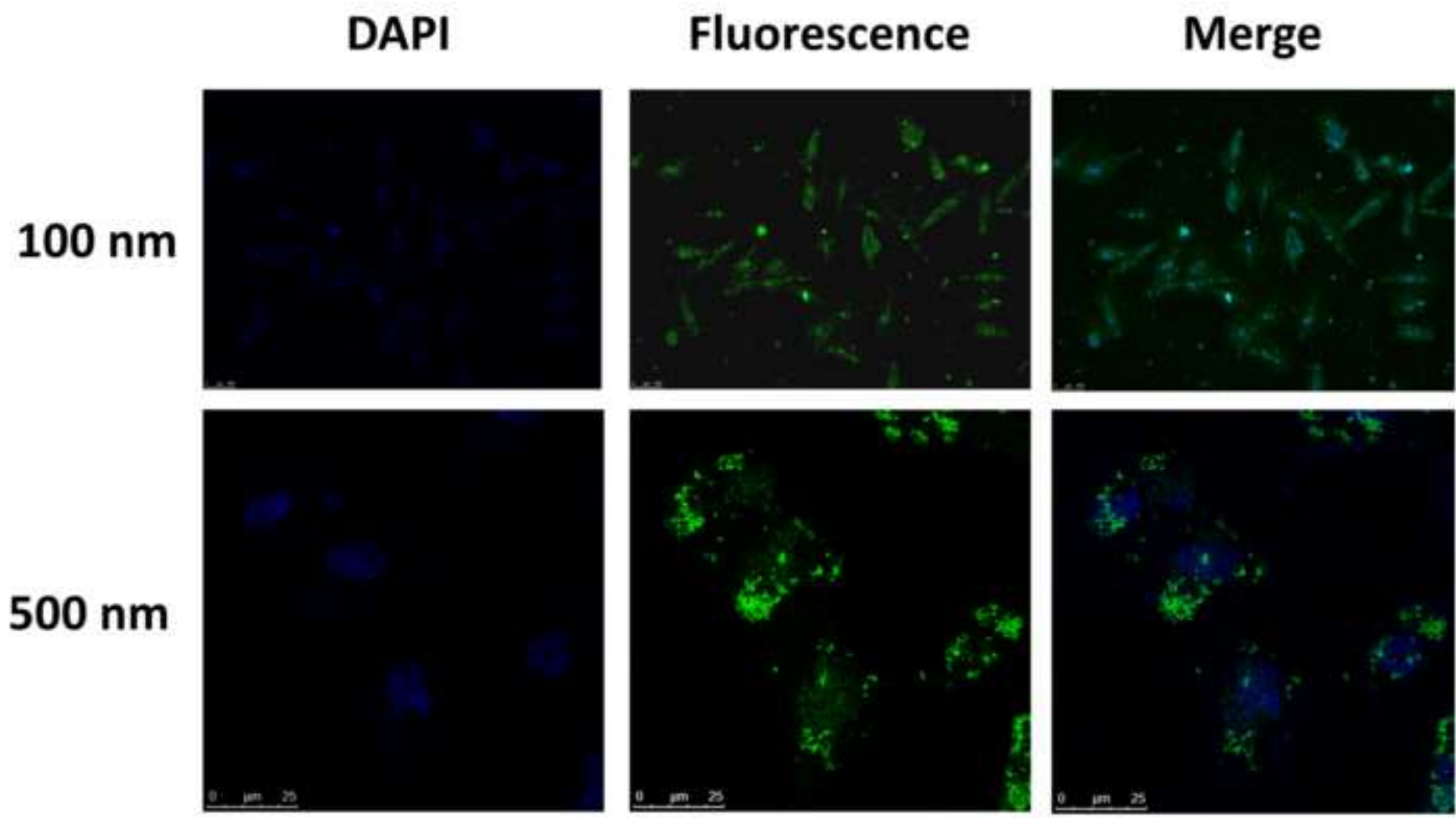


Figure 10

